JOURNAL OF GEOPHYSICAL RESEARCH: SOLID EARTH, VOL. 118, 1–24, doi:10.1002/jgrb.50255, 2013

Magnetotelluric constraints on the fluid content in the upper mantle beneath the southern Canadian Cordillera: Implications for rheology

Dennis Rippe,[1] Martyn J. Unsworth,[1,2] and Claire A. Currie [1]

Received 16 May 2013; accepted 10 June 2013.

[1] Long-period magnetotelluric data were collected on two parallel profiles extending across the southern Canadian Cordillera and used to derive models of the electrical resistivity of the crust and mantle from the Cascadia subduction zone to the Alberta Basin. In the fore arc, the resistivity models indicate an east dipping conductor and conductive mantle wedge, caused by the release of aqueous fluids from the Juan de Fuca plate. Low resistivities are also found beneath the volcanic arc, associated with water released from the subducting slab and mantle melts. Low resistivities in the back-arc upper mantle at depths less than 60 km suggest a shallow asthenosphere compared to the adjacent North American craton where the lithosphere-asthenosphere boundary is at ~200 km. The resistivity of the back-arc upper mantle was interpreted using geotherms, laboratory studies of mineral properties and melting points to determine the type and quantity of fluids present. The low resistivities in the back-arc upper mantle require aqueous fluids, with water content increasing from 0.005 wt % at 50 km to 0.03 wt % at 150 km depth. In addition, melt fractions of up to 1.5% are required at depths less than ~135 km to explain the observed resistivities. The presence of these quantities of aqueous fluids and partial melt will lower the viscosity of the upper mantle, as required by geodynamic models that include vigorous convection in the back arc to explain the observed heat flow.

Citation: Rippe, D., M. J. Unsworth, and C. A. Currie (2013), Magnetotelluric constraints on the fluid content in the upper mantle beneath the southern Canadian Cordillera: Implications for rheology, *J. Geophys. Res. Solid Earth*, *118*, doi:10.1002/jgrb.50255.

1. Introduction

[2] Subduction zones are convergent plate boundaries where a number of important tectonic processes occur. They play a major role in the growth of the continents through (a) providing a mechanism to generate rocks with intermediate to felsic composition from mafic mantle rocks through arc volcanism, (b) initiation of continent-continent collisions, and (c) continental growth through terrane accretion. In addition, subduction zones play an important role in transporting fluids from the surface into the crust and mantle where they control both the physical and chemical properties of the rocks [e.g., *Rüpke et al*., 2004]. At shallow depths (< 15 km), these fluids are released by compaction of the pore space of the subducting oceanic crust, while at greater depths, fluids are released by metamorphic dehydration reactions of hydrous minerals within the slab [*Hacker*, 2008]. The Cascadia subduction zone is one of the best studied subduction zones, where the oceanic Juan de Fuca plate is being subducted beneath the continental part of the North American plate (Figure 1). The Cascadia subduction zone forms the western boundary of the southern Canadian Cordillera, an area of extensive mountain ranges and plateaus, which extends as far east as the Canadian Rocky Mountains and is comprised of five morphological belts [*Monger and Price*, 2002]. From east to west, these belts are the Foreland Belt, Omineca Belt, Intermontane Belt, Coastal Belt, and Insular Belt. The fore-arc region of the Cascadia subduction zone extends from the offshore accretionary prism to the volcanic arc in the Coastal Belt. East of the volcanic arc is the back-arc region, which extends to the Rocky Mountain Trench between the Omineca and Foreland Belts [e.g., *Hyndman and Lewis*, 1999] (Figure 1).

[3] Previous geophysical research has shown that the back-arc mantle of the Cascadia subduction zone is unusually hot, despite the cooling effect of the subducting Juan de Fuca plate [*Hyndman and Lewis*, 1999; *Currie and Hyndman*, 2006]. Elevated mantle temperatures extend several hundred kilometers into the back-arc and cannot be explained by simple subduction-driven mantle wedge corner flow [*Currie et al*., 2004]. Instead, heat transport from the deep mantle through ambient mantle upwelling [*Gough*, 1986] or vigorous, small-scale convection of a weak, low-viscosity asthenosphere [*Currie et al*., 2004] is required to explain the high temperatures in the back arc.

[1]Department of Physics, University of Alberta, Edmonton, Alberta, Canada.
[2]Department of Earth and Atmospheric Sciences, University of Alberta, Edmonton, Alberta, Canada.

Corresponding author: D. Rippe, Department of Physics, University of Alberta, Edmonton, AB T6G 2E1, Canada. (dennis.rippe@ualberta.ca)

2169-9313/13/10.1002/jgrb.50255

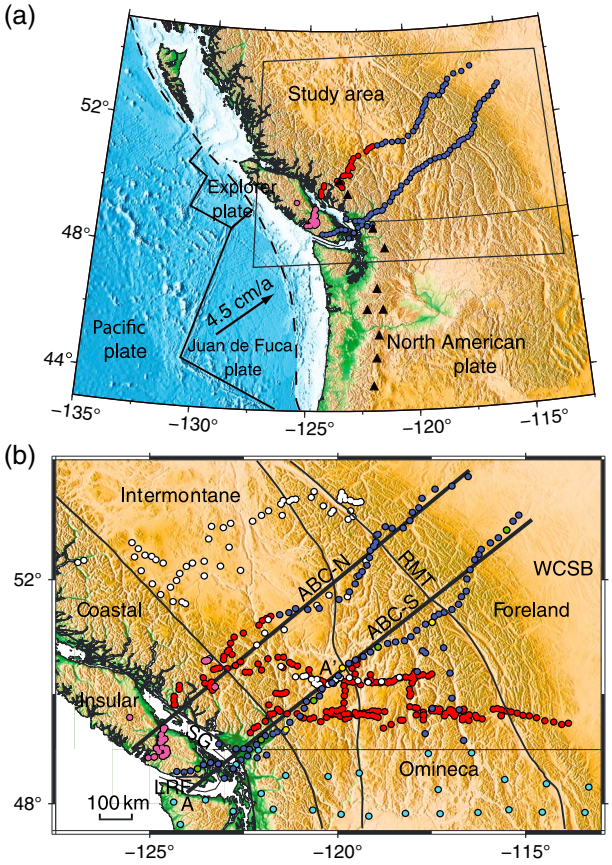

Figure 1. (a) Topography map of the Canadian Cordillera, including locations of two long-period MT profiles. Triangles show major Quaternary volcanoes. (b) Detailed map of the study area, showing morphological belts and available MT data. Blue: long-period MT data (University of Alberta); white: broadband MT data [*Gough*, 1986]; red: broadband MT data (Lithoprobe); pink: broadband MT data [*Kurtz et al.*, 1990]; turquoise: long-period MT data (US-Array). Green dots indicate the locations of the MT stations shown in Figure 6. Yellow dots indicate the locations used for the analysis in section 8. A-A′ is the profile presented by *Soyer and Unsworth* [2006]. SG: Strait of Georgia; LRF: Leech River Fault; RMT: Rocky Mountain Trench; WCSB: Western Canadian Sedimentary Basin.

[4] To understand the pattern of mantle flow in the back arc, it is necessary to constrain the rheology of the upper mantle in the back arc region. Mantle rheology is determined by the composition, temperature, and presence of fluid phases [*Bürgmann and Dresen*, 2008, and references therein]. The presence of aqueous fluids has a profound effect on deformation processes by (a) lowering the strength of the rock for temperatures below the solidus and (b) decreasing the melting point (solidus temperature) of the mantle and causing partial melting [*Hirschmann et al.*, 2009]. Partial melting then lowers the viscosity of the rocks and enhances ductile deformation of the upper mantle [*Kohlstedt and Zimmerman*, 1996, and references therein]. A reduced viscosity related to fluids or partial melt would favor vigorous convection of the back-arc mantle.

[5] Electrical resistivities determined from magnetotelluric (MT) studies are inherently sensitive to the presence of partial melt and also to aqueous fluids, present in either the pore space or dissociated ions (H+) in nominally anhydrous minerals [*Unsworth and Rondenay*, 2013]. Thus, MT studies provide an effective tool to study the fluid content of the upper mantle, which is important for constraining mantle viscosity. Previous broadband MT studies of the Cascadia subduction zone and the Canadian Cordillera have determined the electrical resistivity structure of the crust [*Gough*, 1986; *Ledo and Jones*, 2001], but the lack of long-period MT data has prevented imaging of the upper mantle. The first long-period MT study of the Southern Canadian Cordillera was described by *Soyer and Unsworth* [2006]. In this paper, an extension of this data set is presented, with data extending from the Pacific Ocean to the North American craton in Alberta (ABC-S line, Figure 1b). In addition, long-period MT data collected along an additional profile crossing the Canadian Cordillera to the north are presented (ABC-N line). These data are used to generate 2-D electrical resistivity models. The nonuniqueness in the interpretation of the electrical resistivity models is reduced by interpreting the MT derived resistivity models with independent measurements of subsurface temperature and thermodynamic calculations of the mantle solidus temperature in the presence of water [*Hirschmann et al.*, 2009]. The results are used to constrain the mantle composition and determine the type and quantity of fluids present in the back-arc upper mantle beneath the Southern Canadian Cordillera.

2. Previous Geophysical Observations of the Cascadia Subduction Zone and Canadian Cordillera

2.1. Surface Heat Flow

[6] The Canadian Cordillera is characterized by an elevated surface heat flow compared to the adjacent North American craton east of the Rocky Mountain Trench (RMT) [*Hyndman and Lewis*, 1999; *Currie et al.*, 2004; *Currie and Hyndman*, 2006]. The fore-arc region shows a low heat flow (30–40 mW /m^2), associated with the cooling effect of the subducting Juan de Fuca plate [*Lewis et al.*, 1988]. Temperatures are expected to be <700°C at a depth of 40–60 km [*Hyndman and Peacock*, 2003, *Wada et al.*, 2008], consistent with the stability field of serpentine in the fore-arc mantle wedge. The volcanic arc is characterized by a regional surface heat flow of ~80 mW/m^2, but the local surface heat flow is locally higher near volcanic centers. Farther east, surface heat flow in the back arc increases from ~70 mW/m^2 in the Intermontane Belt to >100 mW/m^2 in the eastern Omineca Belt [*Lewis et al.*, 1992; *Hyndman and Lewis*, 1999], associated with an increase in radiogenic heat production and crustal extension.

[7] In contrast to the heat flow measured at the surface, the reduced mantle heat flow for the back-arc region (i.e., after removing the effect of radiogenic heat production in the crust) is a relatively constant [*Currie et al.*, 2004; *Currie and Hyndman*, 2006]. After correcting for variations in crustal radiogenic heat production, the surface heat flow for the back arc is 75 ± 15 mW/m^2 [*Currie et al.*, 2004]. This is significantly higher than the average heat flow of 42 ± 10 mW/m^2 for the North American craton [*Rudnick et al.*, 1998]. This suggests relatively uniform but unusually

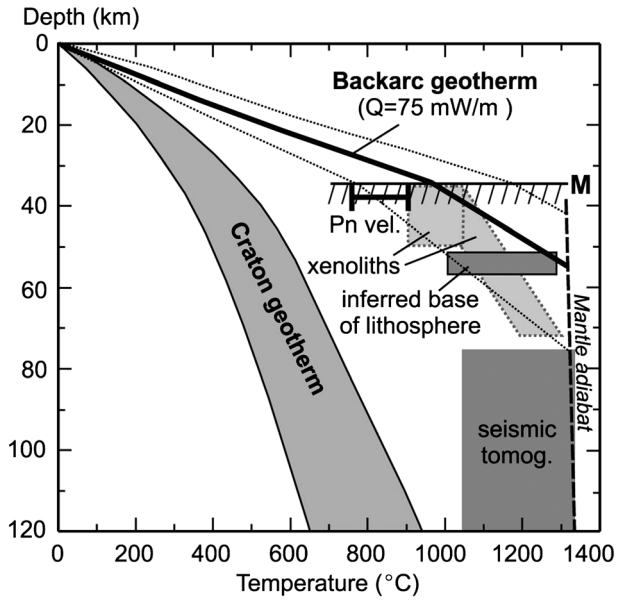

Figure 2. Geotherms for the back arc of the Canadian Cordillera (dotted lines represent 20% uncertainty) and the North American craton derived from surface heatflow data. Additional temperature constraints derived from seismic refraction, seismic tomography, and mantle xenolith thermobarometry data. From *Currie and Hyndman* [2006], reprinted by permission.

high mantle temperatures in the back-arc mantle compared to the North American Craton (Figure 2). The thermal boundary between these two regions is located at the Rocky Mountain Trench, with changes occurring over a distance of less than 200 km [*Hyndman and Lewis*, 1999].

2.2. Mantle Xenolith Thermobarometry

[8] Thermobarometry studies of mantle xenoliths provide another way of constraining the mantle temperatures in the source region of the xenoliths. By analyzing the mineral assemblages and textures of the xenoliths, it is possible to determine the pressure and temperature conditions at which the xenolith last reached chemical equilibrium. Peridotite xenoliths from the southern Canadian Cordillera indicate mantle temperatures between 1000°C at 40 km depth and 1300°C at 60 to 70 km depth (Figure 2) [*Ross*, 1983]. These results are in good agreement with more recent studies of mantle xenolith from this region, which suggest mantle temperatures of 900–1040°C at depths of 38–50 km [*Saruwatari et al*., 2001].

2.3. Effective Elastic Thickness and Density

[9] The effective elastic thickness (T_e) of the lithosphere is mainly controlled by temperature and can be estimated by inferring the surface flexure from gravity and topography data. For the North American craton, the elastic thickness is generally greater than 80 km, indicating low upper mantle temperatures (~600°C at 80 km depth). In contrast, for the Canadian Cordillera, the effective elastic thickness is generally less than 20 km, suggesting higher crustal temperatures, with estimates between 400°C and 600°C at 20 km depth [*Hyndman et al*., 2009].

[10] In addition, crustal thickness and topography data can be used to estimate uppermost mantle temperatures as mantle density decreases with increasing temperature. The North American craton is characterized by a thick crust (~40 km) in combination with low elevation (< 500 m), consistent with cold upper mantle temperatures. In contrast, most of the Canadian Cordillera has a thin crust (32–35 km) in combination with high elevations (1500–2000 m), consistent with high mantle temperatures in this region [*Hyndman and Currie*, 2011].

2.4. Seismic Studies

[11] Seismic velocities of the upper mantle can be measured using seismic refraction and seismic tomography and for common mantle compositions are primarily controlled by temperature and, to a lesser extent, composition [e.g., *Cammarano et al*., 2003]. Elevated temperatures, the presence of fluids, and partial melts generally decrease seismic velocities. Seismic refraction studies in the Southern Cordillera report the continental Moho in the back arc at a depth of 35 km [*Clowes et al*., 1995; *Cook et al*., 2010]. The lithospheric thickness beneath the back arc is estimated to be 50–60 km based on wide angle reflection data [*Clowes et al*., 1995; *Cook et al*., 2004], consistent with temperature estimates of 1300°C at the base of the lithosphere predicted by conductive geotherms for a heatflow of 75 mW/m^2 (Figure 2) [*Chapman*, 1986].

[12] Based on a comparison of seismic refraction data and the thermal lithospheric structure in North America, *Black and Braile* [1982] derived a relationship between the uppermost mantle velocity P_n in kilometer per second and Moho temperature T_m in degree Celcius:

$$P_n = 8.456 - 0.000729\ T_m \quad (1)$$

[13] For the Southern Canadian Cordillera, seismic refraction studies report P_n velocities of 7.7–7.9 km/s in the Intermontane and Omineca Belts, corresponding to Moho temperatures of 750°C to 1050°C. Beneath the volcanic arc, P_n velocities are as low as 7.6 km/s, corresponding to Moho temperatures of 1175°C. In contrast, P_n velocities of 8.1–8.2 km/s are reported for the Archean North American craton [*Christensen and Mooney*, 1995], corresponding to Moho temperatures of 350–490°C. The overall uncertainty in Moho temperature derived from P_n velocity is expected to be of the order ±150°C due to uncertainties in the temperature coefficients as well as anisotropy and compositional variations [*Currie and Hyndman*, 2006, and references therein].

[14] Unusually high upper mantle temperatures in the back arc, compared to the North American craton, are also suggested by seismic tomography, which indicates slower seismic velocities for the back-arc mantle (1–3% for P waves, 3–8% for *S* waves) [e.g., *Frederiksen et al*., 2001; *van der Lee and Frederiksen*, 2005; *Mercier et al*., 2009] compared to global average mantle velocities. Beneath the Archean craton, the mantle shows faster than average velocities (2–3% for *P* waves, 3–4% for *S* waves) [e.g., *Frederiksen et al*., 2001; *van der Lee and Frederiksen*, 2005; *Mercier et al*., 2009]. Whereas both seismic refraction and seismic tomography studies indicate elevated mantle temperatures in the back arc (Figure 2), the reduced

seismic velocities might also be attributed to the presence of fluids, as laboratory measurements indicate that these can reduce seismic velocities primarily by enhancing the anelasticity of the rock [*Karato*, 2006].

2.5. Geodynamic Models

[15] The previously discussed geophysical observations indicate unusually high temperatures in the back-arc mantle compared to the North American Craton despite the cooling effect of the subducting Juan de Fuca plate. Geodynamic modeling indicates that frictional heating along the surface of the subducting slab and latent heat associated with metamorphism in the fore arc produce only a fraction of the heat required to explain these temperatures, so additional heat transport through mantle flow is necessary to explain the observations [*Currie et al*., 2004]. It is significant that the high mantle temperatures extend several hundred kilometers eastward into the back-arc region. In previous studies of back-arc basins, elevated temperatures have often been interpreted as the result of crustal extension [e.g., *Watanabe et al*., 1977]. However, the last episode of extension in the southern Canadian Cordillera occurred during the Eocene and was relatively short lived (< 10 Ma) and spatially limited to a small region in the eastern Omineca Belt, with no evidence for regional extension after this time [*Monger and Price*, 2002]. A comparison with other subduction zone back arcs suggests that high temperatures in the back-arc mantle are common for most subduction zones [*Currie and Hyndman*, 2006]. Geodynamic modeling indicates that these high temperatures are not consistent with simple slab-driven corner flow, in which material from the mantle wedge is entrained and carried downward with the subducting plate and then gets replaced by hot mantle from the back arc [*Currie et al*., 2004]. Instead, heat needs to be carried up through ambient mantle upwelling [*Gough*, 1986] or by vigorous mantle convection of a low-viscosity mantle into the back-arc region [*Currie et al*., 2004].

[16] To understand whether a low-viscosity mantle is consistent with the geophysical observations, it is necessary to further constrain the rheology of the back-arc region. While previous geophysical observations have determined the thermal regime of the mantle (see Figure 2 for a summary), additional observations are required to constrain the hydration state of the back-arc mantle and to determine the effect of water and partial melt on mantle viscosity.

3. Magnetotelluric Observations of the Cascadia Subduction Zone and Southern Canadian Cordillera

3.1. Previous Magnetotelluric Studies

[17] Magnetotelluric (MT) data can be used to image the subsurface electrical resistivity structure of the crust and mantle. The depth of investigation increases as the frequency decreases (period increases). Broadband MT data are collected in the period range 0.001–1000 s and typically sample from the surface to midcrustal depths. Long-period MT data measure signals with periods in excess of 10,000 s and sense both crustal and upper mantle structure, depending on the subsurface resistivity structure. The resistivity of crustal and upper mantle rocks is very sensitive to the presence of fluids, and therefore, MT data can be used to infer the distribution of fluids and assess the rheological structure of the crust and upper mantle. Information derived from MT is thus complementary to that obtained from seismic studies, which are also sensitive to the presence of fluids [*Karato*, 2006].

[18] Over the last four decades, a number of electromagnetic studies have been used to investigate the crustal resistivity structure of the Canadian Cordillera and the Cascadia subduction in British Columbia and Alberta. Early broadband MT studies by *Gough* [1986] detected an extensive low-resistivity layer in the midcrust beneath the Intermontane and Omineca Belts but did not record frequencies low enough to image the upper mantle. *Gough* [1986] explained this layer as being due to fluids generated by extensive partial melting of the uppermost mantle that was the result of mantle upwelling.

[19] A broadband MT study of the subduction zone beneath Vancouver Island was described by *Kurtz et al*. [1986] and *Kurtz et al*. [1990]. Here the subducting Juan de Fuca plate dips northeast at an angle of 8–16° [*Riddihough*, 1979; *Spence et al*., 1985]. The MT study detected a northeast-dipping low-resistivity layer in the North American plate just above the top of the subducting plate. This layer was found to be coincident with the so-called E-horizon, a 5–8 km thick set of seismic reflectors associated with the top of the subducting Juan de Fuca plate [*Green et al*., 1986]. *Kurtz et al*. [1986] interpreted the layer to be caused by 1.6–3.6% saline fluids trapped in the North American crust and originating from metamorphic dehydration reactions within the Juan de Fuca plate. *Hyndman* [1988] interpreted the same data and suggested that the fluids were trapped by an impermeable layer associated with silicate precipitation in the North American plate [*Hyndman*, 1988].

[20] Broadband MT measurements were made farther east in the Southern Canadian Cordillera as part of the multidisciplinary Lithoprobe project (Figure 1). Inversion models derived from these broadband MT data show a resistive upper crust overlying a conductive lower crust [*Ledo and Jones*, 2001] consistent with the results of *Gough* [1986]. Electrical resistivities in the lower crust of the Intermontane Belt were found to be between 100 and 300 Ωm and were relatively uniform along strike. In the Omineca Belt, lower crustal resistivities were between 10 and 50 Ωm in the south, increasing by up to 2 orders of magnitude toward the north. *Ledo and Jones* [2001] interpreted the lower crustal resistivities in the southern Omineca Belt to be caused by saline fluids derived from underplating associated with the extension of this region during the Eocene [*Monger and Price*, 2002]. They suggested that variations in the lower crustal resistivities were mainly due to variations in the amount of fluids and their degree of interconnection.

[21] Previous broadband MT studies have successfully mapped the resistivity of the crust of the Southern Canadian Cordillera. However, the lack of long-period MT data means that little is known about the lower crust and upper mantle. *Soyer and Unsworth* [2006] addressed this issue by collecting long-period MT data on a 350 km long SW-NE profile extending from the Pacific Ocean to the Intermontane Belt (A-A′ in Figure 1b). Inversion models derived from these data show a dipping conductive layer beneath Vancouver Island, very similar to that reported by

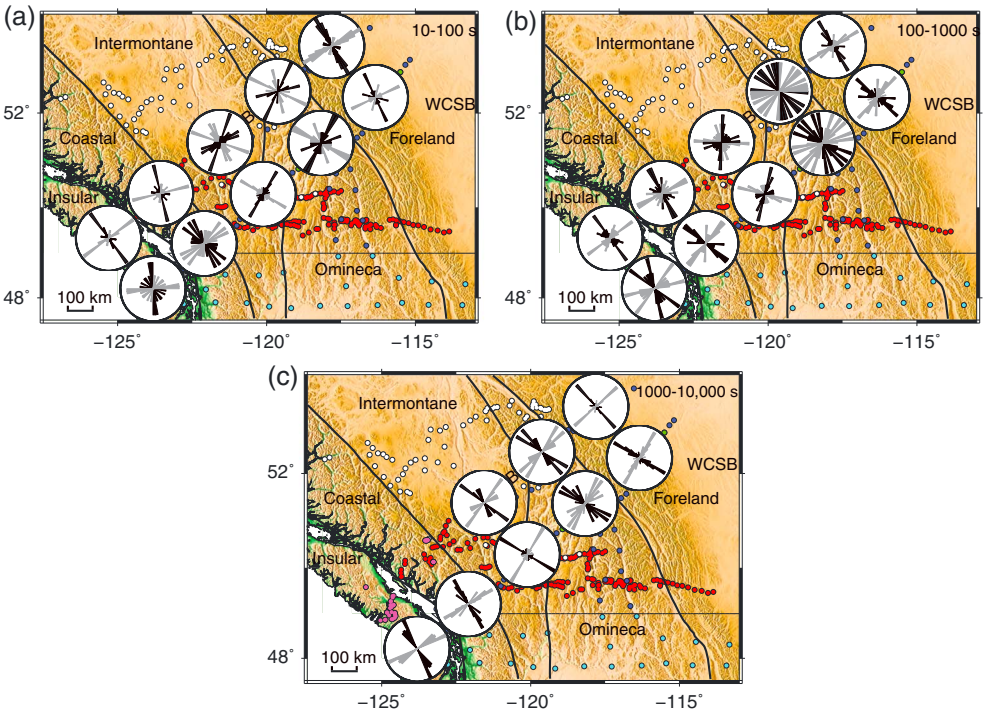

Figure 3. Results of a single site, multifrequency strike analysis for period bands (a) 10–100 s, (b) 100–1000 s, and (c) 1000–10,000 s. Black and white wedges correspond to the two solutions of the strike analysis, as the strike direction contains an inherent 90° ambiguity. The ambiguity was solved by considering the regional geological structure, with the interpreted strike direction plotted as black wedges.

Kurtz et al. [1986]. Farther east, the long-period MT data detected a conductive fore-arc mantle wedge at 50–60 km depth that is spatially coincident with a zone of low seismic velocities. *Soyer and Unsworth* [2006] suggested that the low electrical resistivities and seismic velocities cannot be explained by the presence of serpentinite in the fore-arc mantle but require aqueous fluids with concentration in the range 1–5%.

3.2. New Long-Period Magnetotelluric Observations

[22] The profile of *Soyer and Unsworth* [2006] has provided some information on the electrical resistivity structure of the upper mantle beneath the Southern Canadian Cordillera, but it did not extend across the entire back arc (A-A′ in Figure 1b). It was also limited to a single profile which did not allow along-strike variations in the electrical resistivity of the crust and upper mantle to be investigated. To address these shortcomings, additional long-period magnetotelluric data were collected in 2003 and 2004 at 63 stations with a spacing of ~15 km along the ABC-S profile crossing the entire back arc (Figure 1). Long-period MT data were subsequently collected in 2006 and 2009 at 29 stations on the ABC-N line with a similar interstation spacing (15 km). These data were combined with previously collected Lithoprobe broadband magnetotelluric data to form a second MT profile that crossed the entire extent of the Southern Cordillera. On both transects, the long-period MT data were collected using a combination of LIMS and NIMS instruments in the period range 1–10,000 s. Time series data from both profiles were converted into frequency domain estimates of impedances and transfer functions using the robust, multivariate processing algorithm of *Egbert* [1997]. Coherent noise in the field components was removed using remote reference processing [*Gamble et al*., 1979].

4. Dimensionality of the Long-Period ABC MT Data

4.1. Tensor Decomposition Analysis

[23] Interpretation of MT data requires an understanding of the dimensionality and directionality of the data, and a number of methods have been developed for this task [*Simpson and Bahr*, 2005]. One widely used method is decomposition of the impedance tensor, as originally proposed by *Groom and Bailey* [1989] which represents the measured data as a combination of regional 2-D structure and galvanic (frequency independent) distortion of the electric fields. This method was extended to consider MT data from multiple frequencies and sites by *McNeice and Jones* [2001].

[24] Decomposition of the Southern Canadian Cordillera LMT data began with a single-site, multifrequency analysis. Stations were grouped by location (geological belts), and the tensor decomposition was implemented independently for each site for three period bands (10–100 s, 100–1000 s, and 1000–10,000 s). Rose diagrams of the strike directions obtained for each belt and period band are shown in Figure 3. The strike directions determined from tensor decomposition contain an inherent 90° ambiguity, and the two possible directions are plotted as black and gray wedges. The ambiguity can only be resolved with external information. In this case, the regional geology has a well-defined strike direction (NW-SE) which can remove this ambiguity.

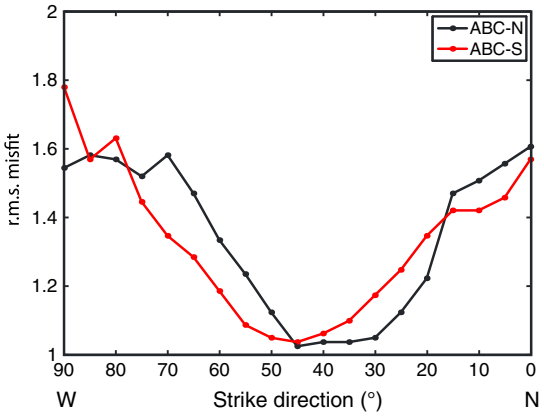

Figure 4. RMS misfit of the tensor decomposition model for a constrained single site, multifrequency strike for a fixed strike direction with data from 100 to 10,000 s for every 5° between North and West.

4.1.1. Strike Direction for the ABC-N Profile (Single Site)

[25] For the ABC-N profile, data in the period bands 10–100 s and 100–1000 s show a strike direction of ~N30° W for both the Insular and Coastal Belts. Farther east, in the Intermontane and Omineca Belts, the strike direction rotates to N15°E to N30°E for the short period band 10–100 s and N-S for the period band 100–1000 s. These directions are consistent with those determined in the study of *Ledo and Jones* [2001]. In the Foreland Belt, the strike direction is N30°W, approximately parallel to the strike of the Canadian Rocky Mountains and western margin of the Western Canadian Sedimentary Basin (WCSB). For the long period band (1000–10,000 s), the strike direction for the Intermontane, Omineca, and Foreland Belts is N60°W to N45°W. This reflects the influence of the coast line, which is of importance at these periods due to the low resistivity of the sea water (0.3 Ωm) [*Parkinson and Jones*, 1979]. No long period data are available for the Insular and Coastal Belts on the ABC-N profile.

4.1.2. Strike Direction for the ABC-S Profile (Single Site)

[26] For the ABC-S profile, the strike direction for the period bands 10–100 s and 100–1000 s in the Insular and Coastal Belts ranges between N45°W and N30°W. The only exception is for the short period band (10–100 s) in the Insular Belt, which exhibits an east-west strike, likely associated with the local strike direction of the Leech River fault on Vancouver Island (Figure 1b). On the ABC-S profile, the strike in the Intermontane and Omineca Belts ranges between N15°E and N30°E, again consistent with *Ledo and Jones* [2001]. The strike direction in the Foreland Belt is N30°W and N45°W for period bands 10–100 s and 100–1000 s, respectively, again parallel to the Canadian Rocky Mountains and margin of the WCSB. For the long period band (1000–10,000 s), the strike direction is N30° W for the Insular and Coastal Belts and N60°W for the Intermontane, Omineca, and Foreland Belts. These long-period strike directions are in good agreement with the strike direction of the coast line. On both profiles, data in the Omineca Belt are highly distorted, most likely due to current channeling [e.g., *Jones*, 1983], and as a result, the strike direction for the period band 100–1000 s is not well defined.

4.1.3. Multisite Strike Direction Analysis

[27] The application of 2-D forward modeling or inversion to MT data requires that a single strike direction is assumed for all the stations and periods included in the analysis. With long profiles, such as those presented in this paper, there are along-profile variations in the strike direction so a multisite decomposition is needed. The single-site analysis described above suggests that the strike direction is in the range N40°W to N50°W. To determine the preferred strike angle in a quantitative manner, a set of decompositions was carried out. In each decomposition the strike direction was fixed and frequency independent distortion parameters calculated for each station over the entire period range. The overall RMS misfit of the predicted to measured impedance tensor was calculated for all stations with data from 100 to 10,000 s. This was repeated for a range of strike directions as shown in Figure 4. For data from 100–10,000 s on the ABC-S profile, the RMS misfit has a minimum centered on a strike direction of N45°W. For the ABC-N profile, the strike analysis has a broad minimum for strike directions between N45°W and N35°W. Therefore, a consistent strike direction of N45°W was preferred for both profiles.

4.2. Induction Vectors

[28] An additional understanding of dimensionality can be obtained from induction vectors which are computed from the magnetic field data. Induction vectors represent the complex ratio of the vertical and horizontal magnetic fields and are associated with lateral variations in conductivity. In the Parkinson convention, the real part of the induction vectors point toward conductive regions, with the magnitude of the induction vector determined by the conductivity gradient [*Parkinson*, 1962]. If the subsurface resistivity is two dimensional, then the induction vectors are perpendicular to the geoelectric strike direction.

[29] Figure 5 shows the real part of the induction vectors using the Parkinson convention for the period bands 10–100 s, 100–1000 s, and 1000–10,000 s. For the short period band (10–100 s), the induction vectors show variability both in direction and magnitude due to local conductivity anomalies in the upper crust. For periods of 100–1000 s, induction vectors in the Insular and Coastal Belts point toward the coast and the low-resistivity ocean. Induction vectors in the Intermontane and Foreland Belts point in opposite directions toward the center of the Omineca Belt, but are slightly disturbed toward the area south of the ABC-S profile. This observation suggests a low-resistivity zone beneath the Omineca Belt, which based on the period range considered, is possibly located in the lower crust or upper mantle. For the long period band 1000–10,000 s, the induction vectors for all stations point toward the low-resistivity ocean, generally decreasing in magnitude with increasing distance from the coast. One exception is the induction vectors in the Foreland Belt, which are similar in magnitude to the induction vectors in the Insular Belt. The increased magnitudes are most likely caused by the combined effect of the low-resistivity ocean [*Parkinson and Jones*, 1979] and a low-resistivity zone extending westward of the Omineca Belt. This idea is supported by the strong suppression of the induction vector magnitudes in the Intermontane Belt.

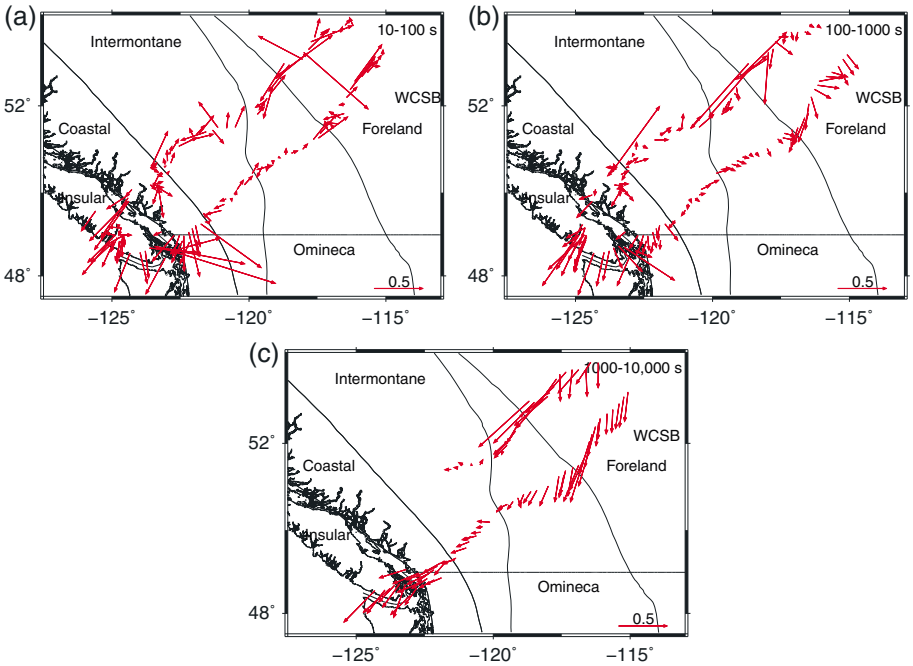

Figure 5. Real parts of the induction vectors using the Parkinson convention [*Parkinson*, 1962] for period bands (a) 10–100 s, (b) 100–1000 s, and (c) 1000–10,000 s.

[30] As the induction vectors for the period bands 100–1000 s and 1000–10,000 s are generally parallel to the profile and perpendicular to the N45°W strike direction determined in the previous section, the magnetic field data also support a two-dimensional analysis of the MT data.

5. Characteristics of the ABC MT Data

5.1. Typical MT Curves

[31] Based on the results of the strike analysis, the undecomposed MT data for the ABC-N and ABC-S profiles were rotated to a strike direction of N45°W. Representative apparent resistivity and phase curves are shown in Figure 6 at the stations indicated in Figure 1. Assuming a two-dimensional subsurface structure, the data can be separated into two independent modes: (a) transverse electric (TE) mode with the electric field parallel to the geological strike and (b) transverse magnetic (TM) mode with the magnetic field parallel to the geological strike. Apparent resistivity and phase angle are related through a Hilbert transform, where an increase in apparent resistivity is associated with a phase less than 45° and a decrease in apparent resistivity is associated with a phase greater than 45°. The absolute values of apparent resistivity can be affected by galvanic distortion, and therefore, only changes in apparent resistivity will be discussed. To account for this galvanic distortion, the inversion presented in section 6 was carried out allowing for static shifts of the apparent resistivity curves.

[32] In the Insular Belt (station ABC-106), the MT data are characterized by a decrease in apparent resistivity with increasing period in both modes at periods less than 100 s. This decrease in apparent resistivity is associated with increasing sensitivity to the low resistivity of the Pacific Ocean. At periods greater than 100 s, the data show an increase in apparent resistivity. The increase in apparent resistivity is more prominent in the TM mode, causing lower phases in the TM mode than in the TE mode. This observation is a result of the coast effect with currents induced in the ocean flowing onshore [*Parkinson and Jones*, 1979].

[33] In the Coastal Belt (station ABC-120), the TE mode is characterized by a decrease in apparent resistivity with period, while the TM mode shows a general increase in apparent resistivity with period. This observation can again be attributed to the coast effect.

[34] In the Intermontane Belt (station ABC-140) and Omineca Belt (station ABC-160), both modes generally show a decrease in apparent resistivity with increasing period, consistent with a decrease in resistivity as the MT data begin to sample the low-resistivity lower crust, as observed by *Ledo and Jones* [2001], and upper mantle. At periods greater than 1000 s in the Omineca Belt, the TE mode shows an increase in apparent resistivity.

[35] In the Foreland Belt (station ABC-204), the data show low apparent resistivities at periods less than 10 s in both modes, associated with the low resistivities of the sedimentary rocks in the WCSB. At periods in the range 10–1000 s, the data show an increase in apparent resistivity. This is likely associated with crystalline basement rocks. At periods greater than 1000 s, the data are characterized by a decrease in apparent resistivity, associated with the low resistivities of the asthenosphere. At all stations, the phases are consistent with the apparent resistivity data, with phases less than 45° for an increase and greater than 45° for a decrease in apparent resistivity with period.

5.2. Pseudosections

[36] Pseudosections provide a convenient way of displaying many MT stations on a profile. Figures 7 and 9 show pseudosections for the ABC-N and ABC-S profiles, respectively. White areas indicate stations and/or periods at which no data were collected or at which the data were excluded due to poor data quality. For the ABC-N line,

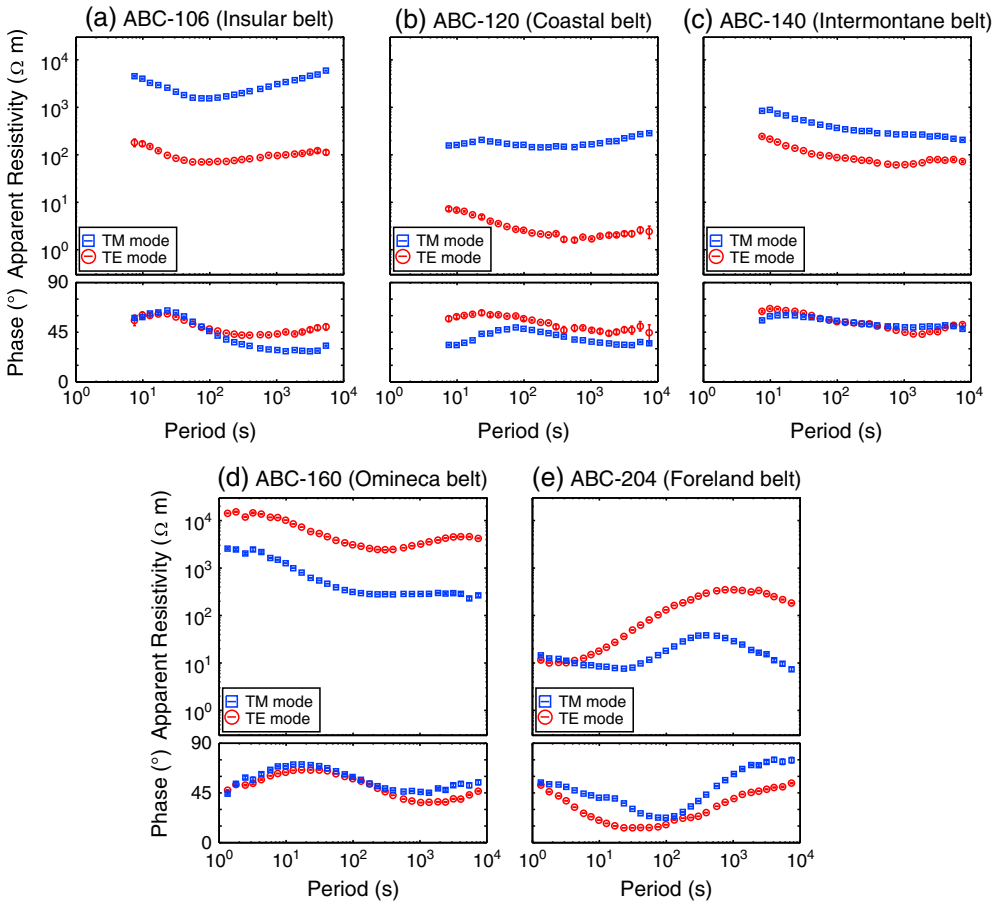

Figure 6. Examples of typical apparent resistivity and phase curves for five MT stations: (a) ABC-106, (b) ABC-120, (c) ABC-140, (d) ABC-160, and (e) ABC-204. MT data were rotated to a strike direction of N45°W. Locations of the MT stations are indicated by green dots in Figure 1.

the TE and TM pseudosections indicate high electrical resistivities at periods less than 100 s in the Insular, Coastal, and western Intermontane Belts. The broadband MT data collected in this region are limited to a maximum period of a few hundred seconds, so no information is available at longer periods. In contrast, on the ABC-S profile, the TE and TM pseudosections indicate lower electrical resistivities at periods less than 100 s in this region than along the ABC-N profile. In addition, a region of low electrical resistivities in the Coastal Belt is observed in the TE mode at periods less than 100 s. Resistivities in this region increase with increasing period. For the eastern Intermontane and Omineca Belts, the TE and TM data indicate a general decrease in resistivity with increasing period, consistent with the decrease in resistivity with depth reported by *Ledo and Jones* [2001]. In the Foreland Belt, the TE data show low resistivities at periods less than 100 s, associated with the low-resistivity sedimentary rocks of the WCSB. Electrical resistivities increase for periods greater than 100 s. The TM data also show the low-resistivity sedimentary rocks of the WCSB as low resistivities at periods less than 100 s. Unlike the TE data, the TM data show another low-resistivity zone for periods greater than 1000 s, extending west underneath the Omineca Belt. The phases for this profile are also consistent with the apparent resistivity data.

6. Inversion of ABC MT Data

[37] The MT data were inverted using the nonlinear conjugate gradient inversion algorithm of *Rodi and Mackie* [2001] to give a 2-D resistivity model. Figure 11 shows resistivity models for the ABC-N and ABC-S profiles, derived from a joint inversion of the TM and TE modes (apparent resistivity and phase) and the vertical magnetic field transfer function data. For reference, the heat flow profile based on the compilation by *Currie and Hyndman* [2006] is plotted. Some stations show TM phases exceeding 90°, most likely caused by channeling of direct currents by localized conductors [e.g., *Jones*, 1983]. At these stations, the TM data were excluded from the inversion, as these out of quadrant phases cannot be fit by the 2-D inversion. For all other MT data, an error floor of 20% in apparent resistivity and 5% in phase (expressed in equivalent apparent resistivity percent, with 5% corresponding to 1.45°) was applied; i.e., data errors that were below these error floor values were set to the error floor. By choosing a larger error floor for the apparent resistivity, less emphasis is put on fitting the apparent resistivity data, as these might be affected by galvanic distortion. In addition, the inversion was allowed to solve for static shifts of the apparent resistivity curves. The error floor for the vertical magnetic fields was set to an absolute magnitude of 0.04. The Pacific Ocean was modeled as a 2.5 km thick layer with a resistivity of 0.3 Ωm.

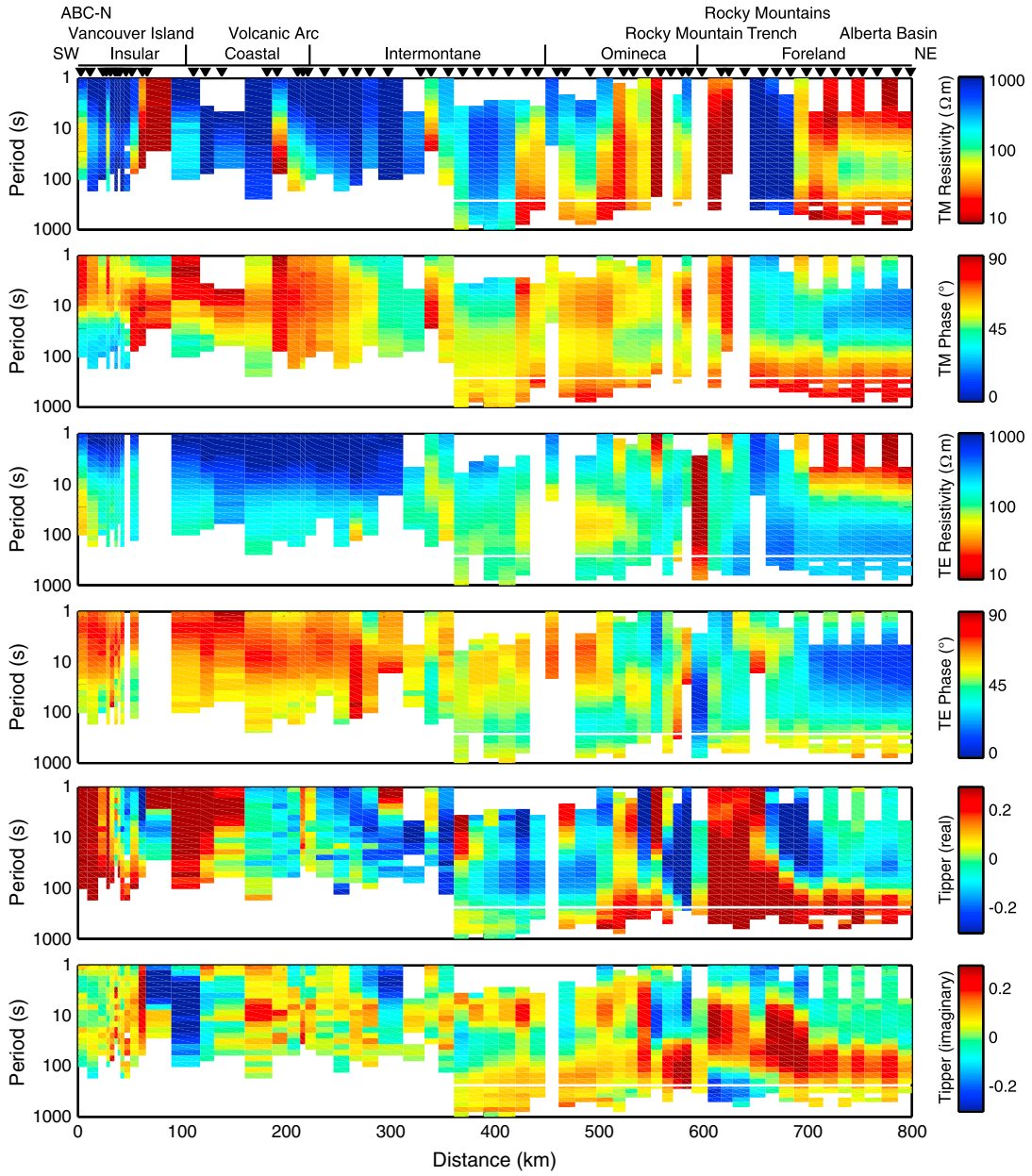

Figure 7. Pseudosections for the ABC-N profile showing the magnetotelluric data for a N45°W coordinate system. The top two panels show the apparent resistivity and phase for the TM mode, the middle two panels show the apparent resistivity and phase for the TE mode, and the bottom two panels show the vertical magnetic field data. White areas correspond to stations and periods with no data.

[38] A smoothing factor $\alpha = 3$ was applied to the horizontal derivatives in the inversion, leading to an increased smoothness in the horizontal direction. The regularization parameter τ provides a trade-off between the overall model roughness and data misfit. Figure 12 shows a plot of model roughness as a function of RMS data misfit for a range of trade-off parameters for both the ABC-N and ABC-S profiles. It can be seen that small τ values produce models with small RMS misfit but large model roughness. Large τ values on the other hand lead to smooth models at the cost of an increased RMS misfit. For the profiles in this study, a regularization parameter $\tau = 3$–10 corresponds to the corner of the L-shaped curve and places equal emphasis on minimizing both the data misfit and the model roughness. The electrical resistivity models obtained for $\tau = 10$ fit the data with an overall RMS data misfit of 2.50 (ABC-N) and 2.34 (ABC-S). The data fit is generally good for both the TM and TE impedance as well as the vertical magnetic field data, as can be seen from a comparison of the data and model responses in Figures 7–10.

7. Interpretation of the ABC Resistivity Models

[39] The electrical resistivity models for the ABC-N and ABC-S profiles shown in Figure 11 are quite similar. In the following section, the common model features as well as differences will be described and interpreted.

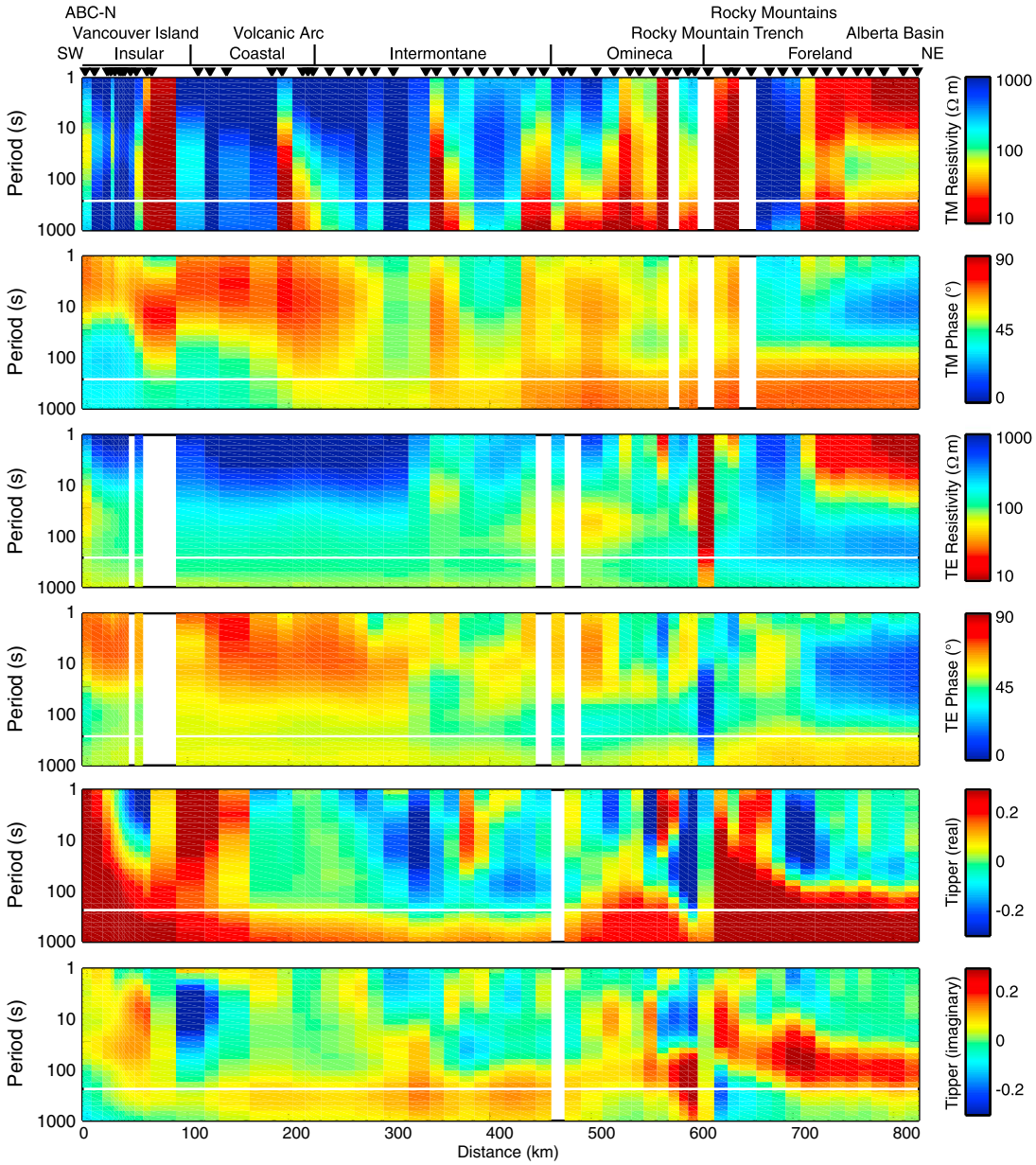

Figure 8. Pseudosections for the ABC-N profile showing the model response of the electrical resistivity model shown in Figure 11. The top two panels show the apparent resistivity and phase for the TM mode, the middle two panels show the apparent resistivity and phase for the TE mode, and the bottom two panels show the vertical magnetic field data. White areas correspond to stations and periods with no data.

7.1. Subduction Zone Conductor ("A")

[40] Beneath the Insular and Coast Belt, both electrical resistivity models show an east dipping, resistive feature that correlates spatially with the subducting Juan de Fuca plate. Above the resistor, both profiles show a conductive feature at a depth of ~20 km in the crust of the North American plate ("A"), dipping east at an angle of ~15° and extending as far east as the Strait of Georgia. It can be shown that MT data can resolve the conductance (conductivity-thickness product) of such a feature. The layer detected in this study has a conductance of 250–300 S and is similar to the conductor reported by *Kurtz et al.* [1990] from an analysis of the same data. Beneath Vancouver Island, the conductor is coincident with a teleseismic low *S* wave velocity zone associated with the top of the subducting Juan de Fuca plate [*Bostock et al.*, 2002; *Nicholson et al.*, 2005]. These observations suggest that the conductor is most likely caused by interconnected aqueous fluids released from the subducting slab and trapped in the crust of the North American Plate (section 3).

7.2. Fore-arc Mantle Wedge ("B")

[41] Another zone of low resistivity (~50 Ωm) is observed at a depth of 30–50 km in the fore-arc mantle wedge and labeled "B." Dry serpentine at mantle temperatures is characterized by high electrical resistivities [*Guo et al.*, 2011; *Reynard et al.*, 2011], so the low-resistivity zone cannot simply be explained by a serpentinized mantle. Instead, an

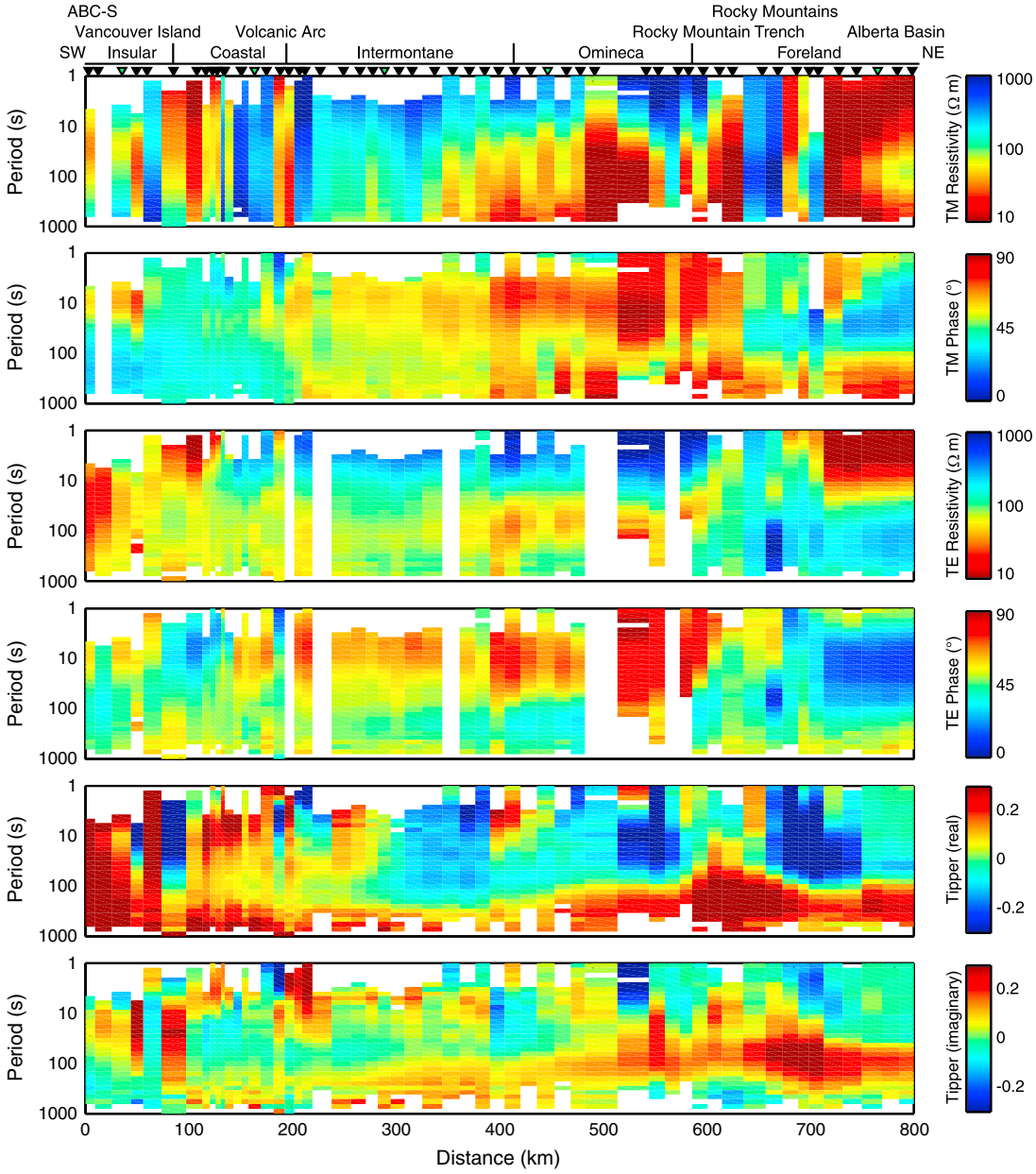

Figure 9. Pseudosections for the ABC-S profile showing the magnetotelluric data for a N45°W coordinate system. The top two panels show the apparent resistivity and phase for the TM mode, the middle two panels show the apparent resistivity and phase for the TE mode, and the bottom two panels show the vertical magnetic field data. White areas correspond to stations and periods with no data.

alternative conductivity mechanism, such as free aqueous fluids, is required to explain the resistivity of this feature [*Soyer and Unsworth*, 2006]. The electrical resistivities in the mantle wedge show significant along-strike variations in resistivity, increasing from ~50 Ωm on the ABC-S profile to ~80 Ωm on the ABC-N profile.

7.3. Volcanic Arc ("C")

[42] Low resistivities are also observed beneath the volcanic arc ("C") extending from the surface of the subducting plate up to crustal depths of 20 km. The low resistivities beneath the volcanic arc are likely due to the fluids released from the subducting slab and the resulting partial melt generated in the mantle wedge that migrates upward to the volcanic arc. Cooling and solidification of this melt within the crust would release water, which may explain the low crustal resistivities in this region [*Soyer and Unsworth*, 2006]. Crustal resistivities increase from ABC-S to ABC-N. Profile ABC-S crosses the volcanic arc close to Mount Baker, while ABC-N crosses to the northwest of the active volcanic arc at Mount Cayley and Mount Meager. This increase of resistivity to the northwest is consistent with the decreasing volcanic activity as the plate boundary changes from a subduction zone to a strike-slip margin.

[43] Magnetotelluric imaging beneath a low-resistivity zone such as the one observed in the lower crust of the ABC-S profile requires care. However, a sensitivity analysis performed by *Soyer and Unsworth* [2006] showed that

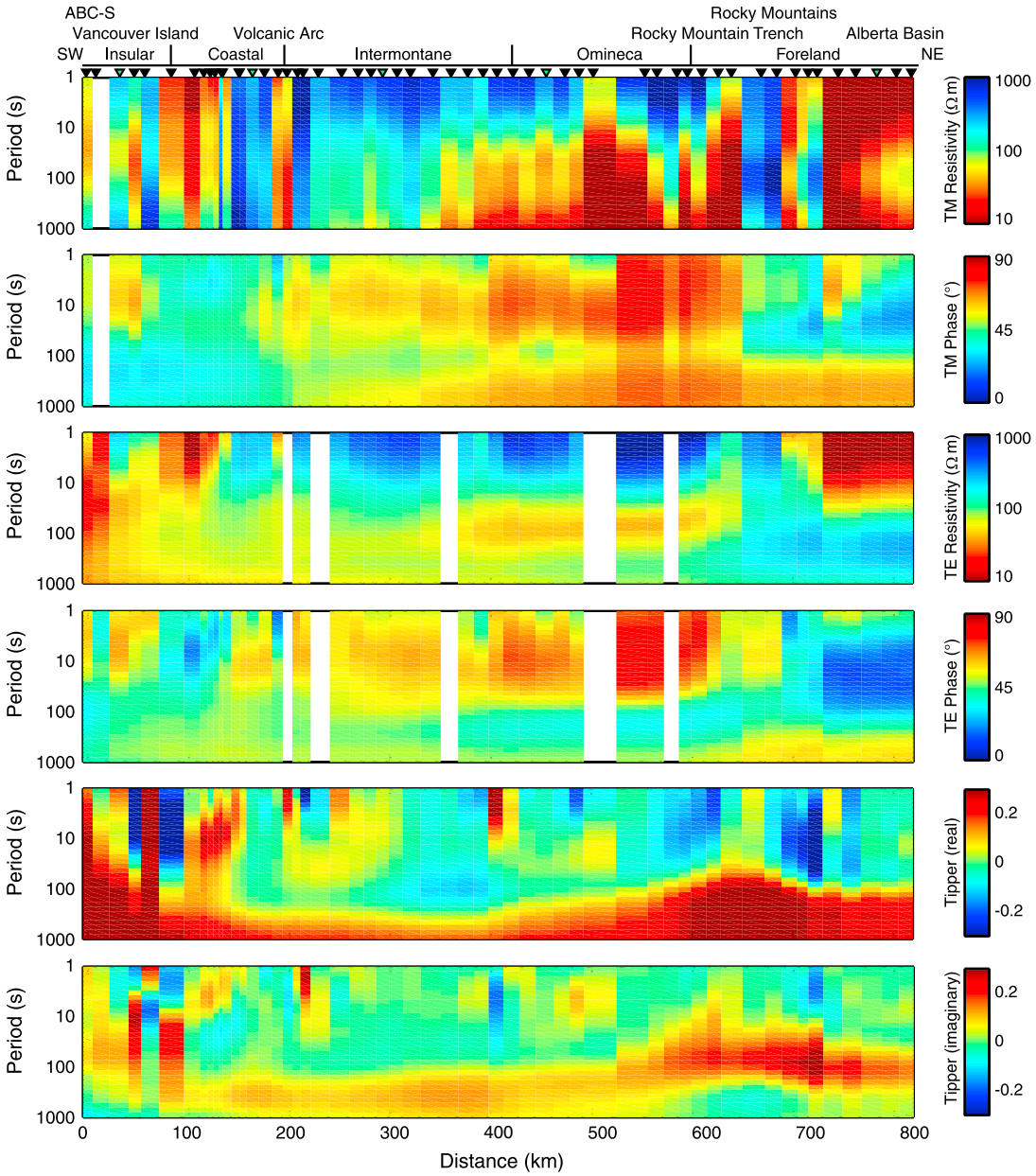

Figure 10. Pseudosections for the ABC-S profile showing the model response of the electrical resistivity model shown in Figure 11. The top two panels show the apparent resistivity and phase for the TM mode, the middle two panels show the apparent resistivity and phase for the TE mode, and the bottom two panels show the vertical magnetic field data. White areas correspond to stations and periods with no data.

low resistivities are required in the mantle beneath the volcanic arc.

7.4. Crustal Conductor ("D")

[44] A crustal conductor is imaged beneath the Intermontane and Omineca Belts ("D") with the top of the conductor located at a depth of ~20 km. Low resistivities are found on the ABC-N profile beneath the eastern part of the Intermontane and the western part of the Omineca Belt. On the ABC-S profile, the low-resistivity crust extends beneath both the Intermontane and Omineca Belts, with the lowest resistivities found beneath the Omineca Belt. The resistivities beneath the Omineca Belt show a general northwest-southeast decrease along strike, in agreement with observations by *Jones and Gough* [1995] and *Ledo and Jones* [2001]. A possible explanation for the low crustal resistivities are saline fluids introduced into the crust as a result of magmatic input due to mantle upwelling that occurred during Eocene crustal extension [*Ledo and Jones*, 2001]. However, this explanation requires the presence of a hydrated crust without the loss of saline fluids or further hydration since the Eocene. An alternative explanation is the presence of partial melt in the lowermost crust, where temperatures exceed the melting temperature of wet granulitic rocks (800–900°C). Along-strike variations in lower crustal resistivity may be attributed to variations in the amount and interconnection of fluids in the crust. As extension occurred primarily in the southern Omineca belt, the

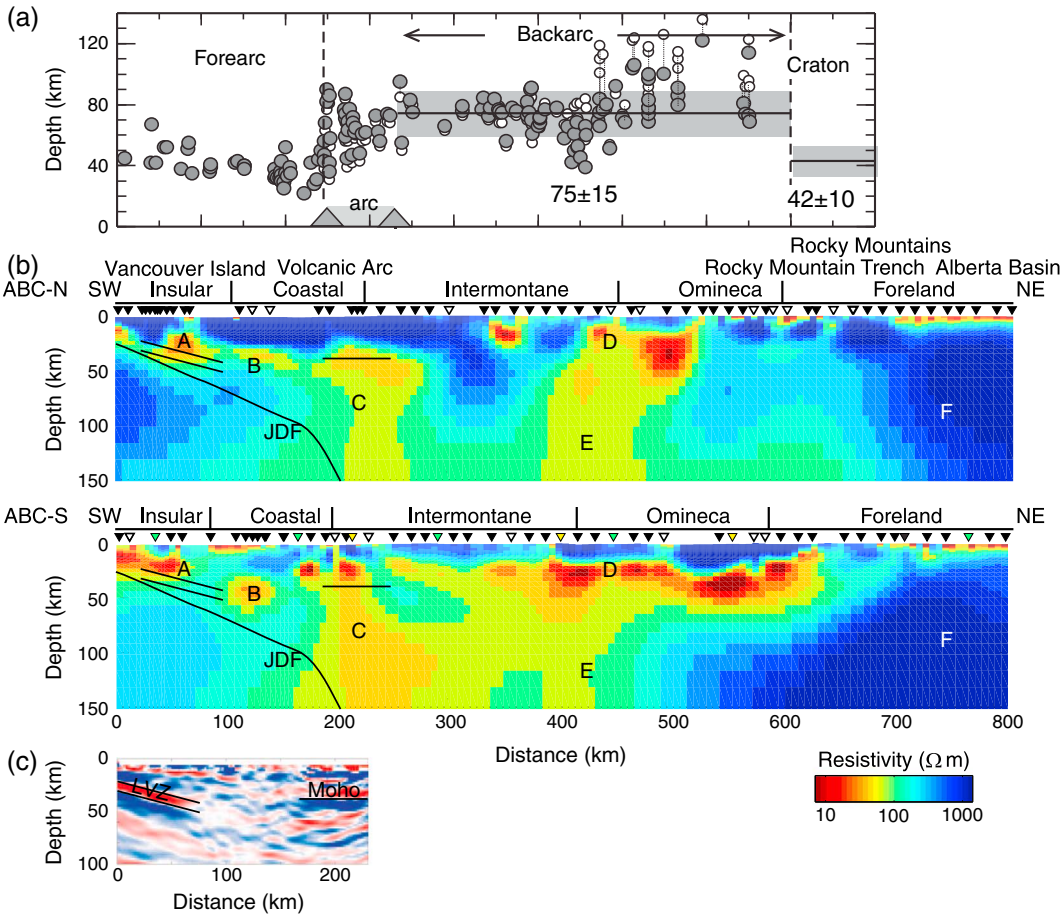

Figure 11. (a) Heat flow profile based on the compilation by *Currie and Hyndman* [2006]. The measured heat flow values (open circles) have been corrected for variations in near-surface heat generation (solid circles). (b) Electrical resistivity models for the (top) ABC-N and (bottom) ABC-S profiles generated using the 2-D nonlinear conjugate gradient inversion algorithm of *Rodi and Mackie* [2001]. A regularization parameter of $\tau = 10$ and a smoothing factor of $\alpha = 3$ were used in the inversions. The electrical resistivity models fit the MT data with an overall RMS misfit of 2.50 (ABC-N) and 2.34 (ABC-S). Black triangles indicate location of MT stations; green triangles indicate the locations of the MT stations shown in Figure 6; yellow triangles indicate the locations used for the analysis in section 8; open triangles indicate the location of MT stations with out of quadrant phases. Black line (JDF) represents top of the subducting Juan de Fuca plate, inferred from seismic refraction data [*Clowes et al*., 1995]. Letters "A" to "E" correspond to model features discussed in section 7. (c) Relative seismic *S* wave velocities from receiver function analysis of *Nicholson et al*. [2005]. A low velocity zone (LVZ) and the continental Moho interface are shown. These features are also superimposed on the electrical resistivity models in Figure 11a.

amount of saline fluids introduced into the crust would be higher in the south compared to the unextended northern Omineca belt. At the same time, shearing of the lower crust during extension could have resulted in an increased horizontal connection of the fluids, thus lowering the resistivity [*Marquis and Hyndman*, 1992].

7.5. Upper Mantle Resistivity Structure ("E" and "F")

[45] The upper mantle shows reduced electrical resistivities (~100 Ωm) in the back arc that extend as far east as the Rocky Mountain Trench at depths greater than 60 km ("E"), suggesting a shallow asthenosphere. As magnetotelluric imaging beneath the crustal conductor ("D") requires care, a sensitivity analysis was conducted, and we will show at the end of this section that reduced upper mantle resistivities are required by the MT data. The reduced resistivity values cannot be explained by dry olivine, unless unrealistic mantle temperatures in excess of 1500°C are assumed (SE03 model in Figure 14). The observed resistivities require an additional conductivity mechanism, such as the presence of hydrogen ions formed from the dissociation of water molecules [*Karato*, 1990]. Another phase that would lower upper mantle resistivity is the presence of partial melt—a process that would be favored by the fact that aqueous fluids will lower the melting temperature of the mantle [*Hirschmann et al*., 2009].

[46] The observed upper mantle resistivity structure, especially the axis of low-resistivity "E," is consistent with mantle upwelling and associated partial melting as proposed by *Gough* [1986]. In addition to lowering the electrical resistivity, the presence of partial melts would also lower the viscosity of the rocks and further enhance ductile

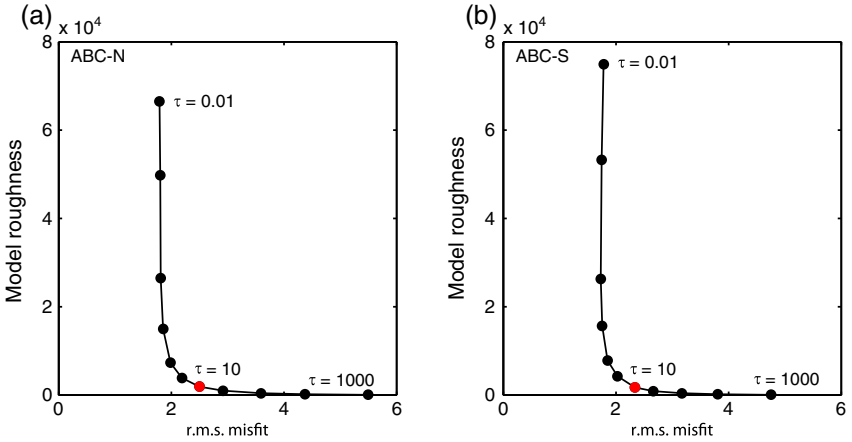

Figure 12. Trade-off curves between model roughness and RMS misfit for (a) the ABC-N line and (b) the ABC-S line. The trade of parameter $\tau = 10$ used in the inversion of the MT data is highlighted in red.

deformation in this region [*Kohlstedt and Zimmerman*, 1996]. In this scenario, the upwelling would be characterized by the low resistivities located beneath the western Intermontane and eastern Omineca Belts, with possible return flow of colder, resistive mantle material occurring beneath the central Intermontane and eastern Omineca belts. Along-strike variations could be indicative of three-dimensional convection patterns associated with additional small-scale convection in this region, as suggested by *Currie et al*. [2004].

[47] The electrical properties of the shallow asthenosphere beneath the Canadian Cordillera are in contrast to the high mantle resistivities (~1000 Ωm) observed beneath the Foreland Belt ("F"). These high resistivities are associated with the lithosphere beneath the North American craton, which extends to depths of ~200 km [*Türkoğlu et al*., 2009]. The ABC-N profile shows a resistivity transition between the Omineca and Foreland Belts, with changes occurring over a distance of ~250 km. This transition is not as sharp as suggested by other geophysical observations, which observe a dramatic change in surface heat flow, elastic thickness, and seismic velocities across the Rocky Mountain Trench (section 2). For the ABC-S profile, the transition is located farther west with highly resistive mantle extending underneath the Omineca Belt at depths greater than 100 km.

[48] A constrained MT inversion was used to test the sensitivity of the MT data to the upper mantle structure beneath the crustal conductor in the Omenica Belt ("D") and how well the MT data could constrain the transition between the low-resistivity back-arc mantle ("E") and the high-resistivity lithosphere of the North American craton ("F"). In particular, for the ABC-S line, it was investigated whether the low mantle resistivities beneath the Omineca Belt could be located in the lower crust instead of the uppermost mantle, with a high-resistivity lithosphere beneath it.

[49] In the constrained inversion, the model resistivities were fixed at a value of 1000 Ωm at depths greater than 50 km beneath the Omineca and Foreland Belts. These resistivities are comparable to the high mantle resistivities observed farther east beneath the Foreland Belt. The same

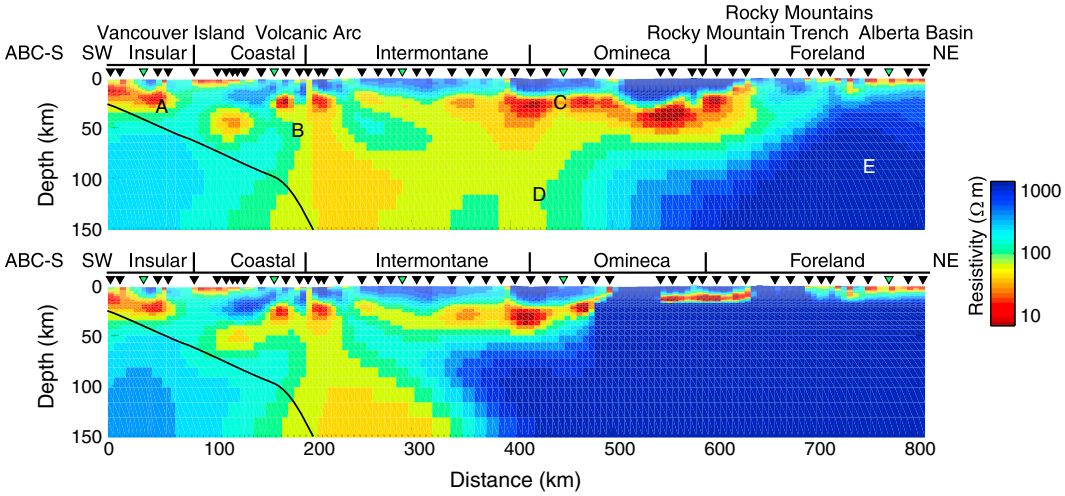

Figure 13. Electrical resistivity model for an (top) unconstrained and (bottom) constrained inversion of the ABC-S data. The electrical resistivity of the constrained model is fixed to 100 Ωm at depths greater than 50 km beneath the Omineca and Foreland Belts. The constrained electrical resistivity model fits the data with an overall RMS misfit of 3.03 compared to an RMS of 2.34 for the unconstrained inversion.

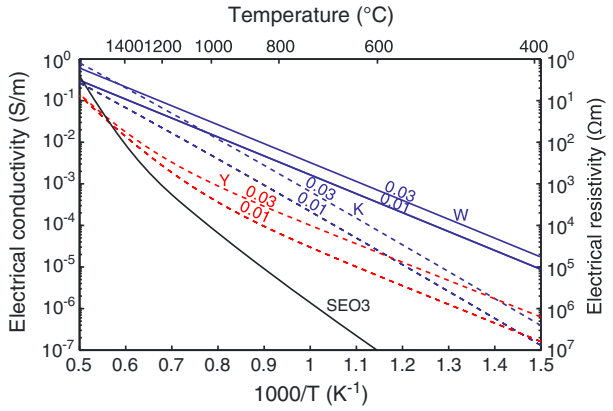

Figure 14. Comparison of the electrical conductivity of olivine as a function of temperature in the presence of 0.01 and 0.03 wt % water as proposed by *Karato* [1990] ("K," blue broken line), and results of laboratory measurements by *Wang et al*. [2006] ("W," blue solid line) and *Yoshino et al*. [2009] ("Y," red broken line). The SEO3 model for dry olivine [*Constable*, 2006] is plotted for comparison (black solid line).

data errors, smoothing factor α, and regularization parameter τ as in section 6 were used in the constrained inversion. With the mantle resistivity fixed at 1000 Ωm, the inversion placed the low resistivities, originally observed in the uppermost mantle, into the crust (Figure 13). The obtained resistivity model fits the data with an RMS misfit of 3.03 compared to an RMS of 2.34 for the unconstrained inversion, which is the result of a significantly worse data fit beneath the Omineca and Foreland Belts. In particular, the constrained inversion is not able to fit the high phases in the TM mode for periods larger than 1000 s. In addition, at these periods the constrained inversion yields vertical magnetic field amplitudes, which are significantly higher than required by the data. These results suggest that low resistivities are required at uppermost mantle depths to explain the measured MT data.

8. Estimation of Water Content and Melt Fraction in the Upper Mantle Beneath the Southern Canadian Cordillera

[50] *Soyer and Unsworth* [2006] showed that the low resistivities in the mantle beneath the ABC-S profile could not be explained by dry olivine. The low resistivity values required either 50–100% hydrogen ion (H+) saturation or up to 4% partial melt. This analysis was limited to the western part of the Canadian Cordillera; in the current study, the entire back arc is considered. *Soyer and Unsworth* [2006] did not address the nonuniqueness associated with the interpretation of low resistivity values observed in the upper mantle, as it is difficult to determine if the reduction in electrical resistivity is due to hydrogen ion (H+) diffusion, partial melts, or a combination thereof. In this paper, we seek to address this nonuniqueness, using knowledge of subsurface temperatures and mineral properties from laboratory studies [*Hirschmann et al*., 2009]. The goal of this analysis is to define regions in which the H+ content is high enough to lower the melting point and allow hydrous melting. In these regions the low resistivity can be explained by a combination of partial melt and hydrogen diffusion. In regions where melting cannot occur, the resistivity must be explained on the basis of hydrogen diffusion alone.

8.1. Estimation of Water Content in the Absence of Partial Melting

[51] The presence of water increases the electrical conductivity of the mantle through several processes, including (a) diffusion of hydrogen ions (H+) formed by the dissociation of water molecules [*Karato*, 1990], (b) increasing the mobility of existing charge carriers, such as Mg^{2+} and Fe^{2+} [*Karato et al*., 1986], and (c) lowering the mantle solidus temperature and causing partial melting [*Hirschmann et al*., 2009]. We first consider whether the observed conductivity can be explained solely by the presence of water (processes (a) and (b)). The effect of (c) will be considered in sections 8.2 and 8.3. To address these points, we will consider three representative MT stations in the back arc region (Figure 15). The analysis is focused on the back arc because the fore-arc mantle is believed to be composed of serpentinite and not olivine [*Hyndman and Peacock*, 2003] and detailed studies of serpentinite conductivity are not available. In this analysis, it should be noted that mantle conductivity depends on both temperature and water content. In our approach mantle temperatures are assumed, and water content is calculated from observed resistivity and laboratory studies of olivine conductivity.

[52] For the temperature model in the back arc, a simplified geotherm was used, with temperatures increasing from 950°C to 1300°C in the lithospheric mantle between depths of 35 and 50 km, respectively. In the asthenosphere, a constant adiabatic gradient of 0.4°C/km was used for depths greater than 50 km. This geotherm is consistent with the inferred regional thermal structure for the Cordillera back arc (Figure 2) [*Currie and Hyndman*, 2006].

[53] Determination of the water content of the mantle also requires a mathematical relationship between resistivity and water content. *Karato* [1990] estimated mantle conductivity from laboratory measurements on hydrogen diffusivity [*Mackwell and Kohlstedt*, 1990] and solubility [*Lizarralde et al*., 1995] in olivine (Figure 14). Laboratory measurements by *Wang et al*. [2006] reported higher conductivities for a given water concentration than the values predicted by *Karato* [1990]. In addition, *Wang et al*. [2006] concluded that diffusion of free protons may contribute to the higher conductivities. More recent laboratory studies by *Yoshino et al*. [2009] reported significantly lower electrical conductivities. *Yoshino et al*. [2009] proposed that the high conductivity values of *Wang et al*. [2006] were caused by dehydration of the olivine sample that resulted in the presence of an interstitial fluid. More details of the calculation are provided in Appendix A.

[54] Figure 15 shows the water content required to account for the observed resistivity beneath three MT stations on the ABC-S profile. It is emphasized that H+ concentration can be expressed in terms of water content, assuming that the water in the mantle is completely dissociated. It can be seen that the required water content generally decreases with depth when the resistivity is approximately constant with respect to depth. This is because increasing temperature is associated with an increase in the diffusivity of the hydrogen ions. Thus, a reduced number of charge carriers are required to explain a given electrical resistivity. The validity of these

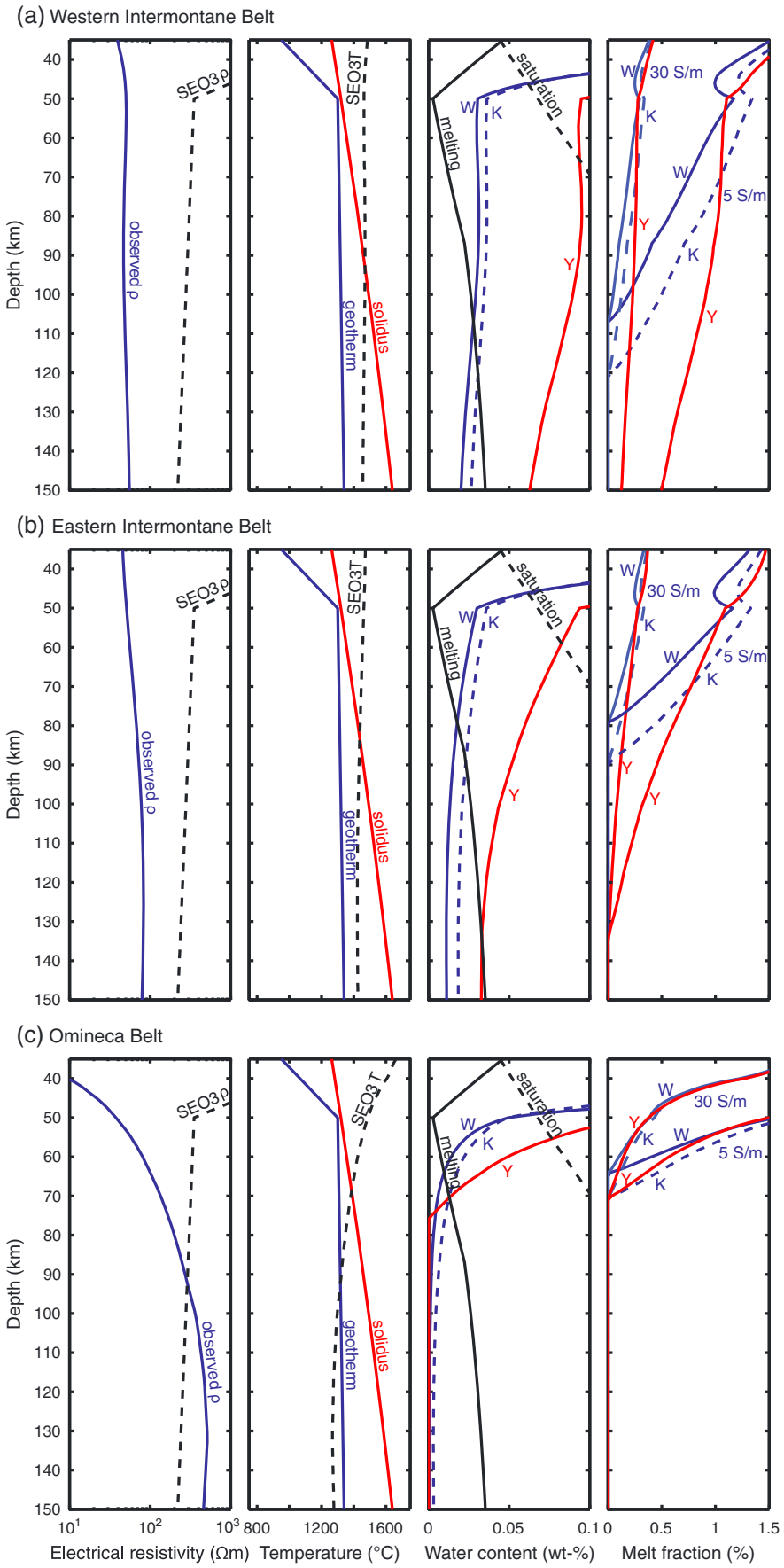
(a) Western Intermontane Belt
(b) Eastern Intermontane Belt
(c) Omineca Belt
Depth (km)
SEO3ρ
observed ρ
SEO3T
geotherm
solidus
saturation
melting
W
K
Y
30 S/m
5 S/m
Electrical resistivity (Ωm)
Temperature (°C)
Water content (wt-%)
Melt fraction (%)

Figure 15

results will be examined by comparing the calculated water content with the solubility limit that is the maximum possible value. The solubility values of *Lizarralde et al*. [1995] were used and were derived from laboratory data collected in the temperature range 1100°C and 1300°C [*Bai and Kohlstedt*, 1992; *Kohlstedt et al*., 1996] using Fourier transform infrared spectroscopy and the uncalibrated spectroscopic method of *Paterson* [1982]. The water solubility was multiplied by a factor of 3.5, as more recent laboratory studies using the spectroscopic method of *Bell et al*. [2003] suggest that the uncalibrated spectroscopic method of *Paterson* [1982] underestimates the water content by a factor of ~3.5.

[55] A key part of this analysis is the equation used to relate H+ concentration and mantle conductivity. As there is no consensus on this, results will be shown for the predictions of *Karato* [1990], *Wang et al*. [2006], and *Yoshino et al*. [2009]. It can be seen that the three estimates of H+ concentration are quite different from one another (Figure 14).

[56] 1. Station ABC-128 is located east of the volcanic arc in the western Intermontane Belt. The electrical resistivity at this site does not vary significantly with depth and is relatively constant (~50 Ωm) and approximately 1 order of magnitude lower than the prediction of the SEO3 model for dry olivine [*Constable*, 2006] for the assumed mantle temperatures. The presence of another conduction mechanism is required to explain the observed electrical resistivities. As can be seen from Figure 15, for depths above 50 km, the results of both *Karato* [1990] and *Wang et al*. [2006] require water contents larger than 0.05 wt %, which are in excess of the water solubility limit. At depths greater than 50 km, a water content of 0.02–0.03 wt % is required to explain the observed electrical resistivity. If the resistivity values are interpreted with the results of *Yoshino et al*. [2009], a much higher water content is required that is greater than 0.1 wt % at depths greater that 65 km. These values exceed the solubility limit and show that hydrogen alone cannot explain the observed combination of resistivity and temperature. For depths greater than 65 km, the required water content decreases from 0.1 to 0.06 wt % at 150 km depth, which is below the water solubility limit. At these depths, hydrogen diffusion alone can explain the observed resistivity.

[57] 2. For station ABC-150 in the eastern Intermontane Belt, electrical resistivities are similar to those at station ABC-128 but increase slightly with depth (from 50 Ωm at 35 km to 80 Ωm at 150 km). At shallow depths, the results are similar to those discussed in (a). The required water content exceeds the water solubility limit at depths less than ~50 km (based on the relationships of *Karato* [1990] and *Wang et al*. [2006]) and 65 km (based on *Yoshino et al*. [2009]). For depths below 50 km, the water content based on *Karato* [1990] and *Wang et al*. [2006] decreases from ~0.03 to ~0.01 wt %. Similarly, for depths greater than 65 km, the water content based on the laboratory measurements by *Yoshino et al*. [2009] decrease from ~0.09 to ~0.03 wt %. These water contents are below the water solubility limit.

[58] 3. Station ABC-174, located in the Omineca belt, shows an increase of resistivity with depth from 10 Ωm at 40 km to 500 Ωm at 150 km. For depths less than ~90 km, the electrical resistivities are below those predicted by the SEO3 model for dry olivine, requiring the presence of fluids. Using the relationships of *Karato* [1990], *Wang et al*. [2006], and *Yoshino et al*. [2009], the required water content exceeds the water solubility limit at depths less than 50–60 km. Below these depths, the water content decreases from 0.06–0.07 wt % to values close to zero at 90 km depth. At depths greater than 90 km, the observed electrical resistivities are in excess of those predicted by the SEO3 model for dry olivine, suggesting that the assumed mantle temperatures are ~50°C too high. This station could provide an example of using electrical resistivities to refine estimates of mantle temperatures, if a dry composition is assumed.

8.2. Effect of Water on the Mantle Solidus Temperature

[59] The previous section showed that relatively high concentrations of H+ are required to explain the observed mantle resistivity beneath the Southern Canadian Cordillera. Such concentrations can potentially reduce the melting temperature of the mantle. In this section, calculations are revised to determine if sufficient H+ is present to permit mantle melting. For a specified water content and depth, it is possible to calculate the reduced solidus temperature and details are listed in Appendix C. Similarly, if the temperature at a certain depth is known, the amount of water that is required to initiate hydrous melting can be calculated, i.e., the amount of water required to reduce the solidus temperature below the actual mantle temperature obtained from geophysical observations, such as the simplified geotherm derived from surface heat flow and other thermal indicators.

[60] To determine the effect of water on hydrous melting of the nominally anhydrous upper mantle, a Tecton (mean spinel peridotite) composition was assumed [*Griffin et al*., 2003]. This composition corresponds to a moderately depleted mantle characteristic of regions for which the last tectonothermal event in the overlying crust occurred in the last 1.0 Ga (based on the classification of *Griffin et al*. [2003]). The partition coefficients for the mantle minerals were taken from a compilation by *Hirschmann et al*.

Figure 15. Electrical resistivities, mantle temperatures water contents, and melt fractions for three stations along the ABC-S profile: (a) ABC-128 in the western Intermontane Belt, (b) ABC-150 in the eastern Intermontane Belt, and (c) ABC-174 in the Omineca belt. Locations of the MT stations are indicated by yellow dots in Figure 1. From left to right: (i) Observed electrical resistivity (blue line) and electrical resistivity predicted by the SEO3 model for dry olivine (black broken line). (ii) Simplified geotherm (blue line), dry peridotite solidus (red line), and temperature required to explain the observed electrical resistivities by the SEO3 model (black broken line). (iii) Water content based on the results by *Karato* [1990] ("K," blue broken line), *Wang et al*. [2006] ("W," blue solid line), and *Yoshino et al*. [2009] ("Y," red line). Water content required for hydrous melting (black solid line). Water solubility limit (black broken line). (iv) Melt fractions based on the results by *Karato* [1990] ("K," blue broken line), *Wang et al*. [2006] ("W," blue solid line), and *Yoshino et al*. [2009] ("Y," red line) for melt conductivities of 5 and 30 S/m.

[2009]. Figure 15 shows the minimum amount of water required for hydrous melting at the temperatures determined from surface heat flow. For the Canadian Cordillera, it can be seen that in the uppermost mantle (35–50 km), the amount of water required for hydrous melting decreases from 0.055 to 0.005 wt %, as the temperature increases from 950°C to 1300°C over this depth range and approaches the dry peridotite solidus. At 50 km depth, the difference between the geotherm and the dry peridotite solidus is ~60°C. At depths greater than 50 km, the temperature difference between the geotherm and the dry solidus increases, requiring larger amounts of water to initiate hydrous melting (~0.03 and 0.04 wt % at 100 and 150 km depth, respectively). At all these depths, these water contents are below the water solubility limit.

8.3. Water Content and Degree of Melting at the Reduced Mantle Solidus

[61] The water content values calculated in section 8.1 may not necessarily reflect the actual composition of the mantle. If the water content is high enough, it can reduce the mantle solidus sufficiently for the mantle to partially melt. By comparing the water content required to explain the electrical resistivity models (section 8.1) with the minimum water content required to initiate melting (section 8.2), it is possible to define the regions where partial melting of the mantle could occur.

[62] If the water content required to explain the electrical resistivity models is insufficient to lower the mantle solidus to temperatures below the simplified geotherm, no hydrous melting is expected. In this case, the observed electrical resistivities must be solely explained by hydrogen diffusion, and the water content values are those presented in section 8.1. If the water content exceeds the amount required to lower the reduced mantle solidus to the inferred temperatures, hydrous melting of the mantle rocks can occur. In this case, the observed electrical resistivities must be explained by a combination of hydrogen diffusion and partial melt.

[63] To perform this analysis, it is necessary to calculate the resistivity of a partially molten rock. This was done using a modification of Archie's law for two conducting phases, as described in Appendix B. The two conducting phases correspond to (1) the wet peridotite mantle, whose electrical conductivity σ_1 can be approximated by hydrous olivine (Appendix A), and (2) the melt with an electrical conductivity σ_2 and a melt fraction χ_2. The conventional form of Archie's Law [*Archie*, 1942] cannot be used, as it only accounts for one conducting phase distributed within a nonconductive phase. For the mantle, the assumption of a nonconductive rock matrix is not valid as thermally activated conduction through the rock matrix is significant at upper mantle temperatures. Typical electrical conductivities for melts (σ_2) range from 1 to 10 S/m for temperatures between 1200°C and 1400°C [*Tyburczy and Waff*, 1983]. Thus, initial calculations used a value of 5 S/m that was in the middle of this range. More recent laboratory studies by *Ni et al*. [2011] have shown that the presence of dissolved water in the melt significantly increases the conductivity. Given that the upper mantle in the study area has a high water content, and that on melting the water is partitioned into the melt, a value of 4 wt % was used, giving a melt conductivity of ~ 30 S/m. Note that higher values of melt conductivity require lower melt fractions to explain an observed mantle conductivity. The degree of interconnection of the melt phase is described by the cementation factor m, with larger values corresponding to a lower degree of interconnection. In this study, a cementation factor $m = 1.3$ for the melt phase was assumed based on laboratory studies of *ten Grotenhuis et al*. [2005].

[64] As the degree of melting as a function of excess water content is unknown, the hydration state and degree of melting can range between two possible end-members:

[65] 1. The electrical resistivity is explained solely by water and no partial melt. This case gives the maximum amount of water required by the electrical resistivity model, as discussed in section 8.1.

[66] 2. The electrical resistivity is explained by a combination of water and partial melt, where the amount of water is equal to the minimum amount of water required to allow hydrous melting, as discussed in section 8.2. In this case, the degree of melting required to explain the data is the maximum amount of melt which is still in agreement with the electrical resistivity model.

[67] The actual water content and melt fraction are expected to be somewhere between these two end-member models. Figure 15 shows the melt fraction required to explain the electrical resistivity models, illustrated for three stations on the ABC-S profile.

[68] 1. At station ABC-128 east of the volcanic arc in the western Intermontane Belt, the required water contents based on the relationships of *Karato* [1990] and *Wang et al*. [2006] exceed the water content required for hydrous melting down to depths of 110–120 km. Therefore, at these depths, the observed electrical resistivities need to be explained by a combination of water and melt. At 35 km depth, melt fractions between 0.4% and ~1.5% are required for melt conductivities of 30 and 5 S/m, respectively. The required melt fraction decreases for both melt conductivities to 0% at 110–120 km depth. Below this depth, the water content is too low to allow hydrous melting. In contrast, the required water content based on the laboratory measurements by *Yoshino et al*. [2009] is sufficient to allow hydrous melting to a depth of 150 km. The corresponding melt fraction decreases from 1.5% at 35 km to 0.5% at 150 km for a melt conductivity of 5 S/m. For a melt conductivity of 30 S/m, lower melt fractions are required decreasing from 0.4% at 35 km to 0.1% at 150 km.

[69] 2. For station ABC-150 in the eastern Intermontane Belt, the water contents based on the relationships of *Karato* [1990] and *Wang et al*. [2006] are sufficient to allow for hydrous melting to depths of 80–90 km. In contrast, based on the laboratory measurements by *Yoshino et al*. [2009], hydrous melting is possible to depths of ~135 km. For a melt conductivity of 5 S/m, the required melt fractions decrease from ~1.25–1.5% at 35 km to 0% at 80–90 km and 135 km depths, respectively. Similarly, for a melt conductivity of 30 S/m, the melt fractions decrease from ~0.35% to 0% over the same depth range. No hydrous melting occurs below these depths.

[70] 3. For station ABC-174 in the Omineca belt, the required water contents based on the relationships of *Karato* [1990] and *Wang et al*. [2006] as well as those by *Yoshino et al*. [2009] are sufficient to allow hydrous melting down to depths of 65–70 km. The corresponding

melt fractions are between 2% and 5% at 35 km for melt conductivities of 30 and 5 S/m, respectively, and decrease to 0% at 65–70 km depth. Below these depths, hydrous melting is not possible.

9. Discussion and Conclusions

[71] The data and analysis presented in this paper have advanced our understanding of the Canadian Cordillera in two distinct ways. They have (a) provided new observations of upper mantle resistivity structure that reveal the extent of low-resistivity material in the back arc upper mantle and (b) attempted to determine if these low resistivities are due to the presence of partial melt or hydrogen ions (water) in the upper mantle.

[72] In terms of (a), the new long-period MT data show a pervasive zone of low resistivity extending across the back arc upper mantle. Within this broad zone, a number of features can be distinguished. A low-resistivity zone originates above the subducting slab at a depth of 100 km beneath the volcanic arc and can be traced to the surface close to active volcanoes. This is clearly associated with fluids released from the subducting slab and the upward migration of melts through the mantle wedge and crust. The electrical resistivity models show low resistivities in the lower crust of the Intermontane and Omineca Belts ("D") that are most likely caused by saline fluids and/or partial melts. Reduced electrical resistivities are observed at depths greater than 60 km ("E") extending into the upper mantle and confirm the suggestion of *Gough* [1986] that the upper mantle upwells in this region. The asthenosphere in this region is clearly much shallower than that in the adjacent North American craton where magnetotelluric and seismic data image the lithosphere-asthenosphere boundary at a depth in excess of 200 km [*Türkoğlu et al*., 2009]. The transition between the low-resistivity back arc and the high-resistivity North American Craton is observed beneath the boundary between Omineca and Foreland Belts on the ABC-N profile. However, this transition appears to be located farther west on the ABC-S profile with highly resistive mantle extending beneath the Omineca Belt at depths greater than 100 km. These spatial variations may indicate complex, small-scale convection as suggested by *Currie et al*. [2004].

[73] The second area in which this study has contributed is (b) in improving our understanding of the composition of the upper mantle. This is important because geodynamic models for this region require relatively low viscosities to permit effective small-scale upper mantle convection that transports high-temperature material across the back arc. A reduced mantle viscosity requires the presence of partial melt and/or elevated concentrations of water, likely present as hydrogen ions. MT studies that generate models of upper mantle resistivity are important in this respect since mantle resistivity is inherently sensitive the presence of these phases. Previous MT studies on the Southern Canadian Cordillera by *Soyer and Unsworth* [2006] showed that the low resistivities in the back-arc mantle could be explained by either hydrogen diffusion, partial melting, or a combination thereof but could not address this nonuniqueness.

[74] This paper has attempted to address this nonuniqueness by using thermal and mineral properties as constraints. This analysis has shown that the electrical resistivity of the upper mantle beneath the volcanic arc is consistent with a composition of hydrated olivine with a water content increasing from 0.005 wt % at 50 km to 0.02–0.04 wt % at 150 km depth on the ABC-S profile. These fluids likely originate in metamorphic dehydration reactions in the subducting slab. This amount of water is sufficient to lower the mantle solidus temperature and allow partial melting of mantle rocks with melt fractions between 0.5 and 2%. Additional water is required at shallow mantle depths (35–135 km) beneath the Intermontane and Omineca Belts, with water content ranging from 0.005 wt % at 50 km to 0.01–0.03 wt % at 150 km on the ABC-S profile. The shallow mantle in this region is also subject to partial melting, with melt fractions decreasing from between 0.4% and ~1.5% at 35 km to 0% at ~135 km depths. A similar analysis of the ABC-N profile shows a decrease in water content and melt fraction toward the northwest.

[75] The presence of water and melt has a significant effect on the rheology of the mantle by lowering its viscosity [*Dixon et al*., 2004]. Based on the rheology laws given by *Dixon et al*. [2004], the inferred water contents of 0.005–0.03 wt % beneath the Intermontane and Omineca Belts imply mantle viscosities between $2.3 \cdot 10^{19}$ and $4.2 \cdot 10^{19}$ Pa s at a depth of 75 km, if the simplified geotherm and a strain rate of 10^{-15} s^{-1} are assumed. These viscosities are significantly lower than values determined for continental shield areas that are in the range 10^{20}–10^{21} Pa s [*Dixon et al*., 2004]. They are sufficiently low to permit vigorous mantle convection [*Honda et al*., 2002]. This type of convection within a low-viscosity mantle could provide a possible explanation for the hot temperatures in the back arc of the Canadian Cordillera [*Currie et al*., 2004].

[76] A major limitation in the presented analysis is the disagreement between the laboratory measurements of *Wang et al*. [2006] and *Yoshino et al*. [2009] on the effect of water on mantle conductivity. Resolving this discrepancy would greatly improve estimates of the quantity and type of fluid present in the upper mantle and will require additional experiments of the electrical properties of upper mantle rocks in the presence of water.

Appendix A: Electrical Resistivity of the Peridotite Mantle in the Presence of Water

A1. Electrical Conductivity of Dry Olivine According to *Constable* [2006]

[77] In the absence of any fluid phases, laboratory measurements indicate that the electrical resistivity of a peridotite mantle is strongly temperature dependent, whereas the effect of pressure is relatively small [*Xu et al*., 2000]. The electrical resistivity is mainly determined by the most common mantle minerals (olivine and pyroxene). Given the dominance of olivine in terms of both volume fraction and electrical resistivity, *Constable* [2006] approximated the resistivity of a dry peridotite mantle to first order by the electrical resistivity of olivine. Taking into account the concentration and mobility of polaron and magnesium vacancies and their dependence on oxygen fugacity, *Constable* [2006] derived a relationship describing

the conductivity of olivine as a function of temperature (SEO3 model):

$$\sigma_{\mathrm{SEO3}} = \left[\mathrm{Fe}^{\bullet}_{\mathrm{Mg}}\right]\mu_{\mathrm{Fe}}e + 2\left[V''_{\mathrm{Mg}}\right]\mu_{\mathrm{Mg}}e \tag{A1}$$

with mobilities

$$\mu_{\mathrm{Fe}} = 12.2\cdot10^{-6}e^{-1.05\mathrm{eV/kT}} \tag{A2}$$

$$\mu_{\mathrm{Mg}} = 2.72\cdot10^{-6}e^{-1.09\mathrm{eV/kT}} \tag{A3}$$

and concentrations

$$\left[\mathrm{Fe}^{\bullet}_{\mathrm{Mg}}\right] = b_{\mathrm{Fe}}(T) + 3.33\cdot10^{24}e^{-0.02\,\mathrm{eV/kT}}f_{\mathrm{O_2}}^{1/6} \tag{A4}$$

$$\left[V''_{\mathrm{Mg}}\right] = b_{\mathrm{Mg}}(T) + 6.21\cdot10^{30}e^{-1.83\,\mathrm{eV/kT}}f_{\mathrm{O_2}}^{1/6} \tag{A5}$$

of the polaron and magnesium vacancies, where e is the electronic charge, T is the temperature, and k is the Boltzmann's constant (in eV/K). b_{Fe} and b_{Mg} are the defect concentrations extrapolated from measurements at temperatures of 1000°C, 1100°C, and 1200°C [*Constable*, 2006]:

$$b_{\mathrm{Fe}}(\mathrm{T}) = 5.06\cdot10^{24}e^{-0.357\ \mathrm{eV/kT}} \tag{A6}$$

$$b_{\mathrm{Mg}}(\mathrm{T}) = 4.58\cdot10^{26}e^{-0.752\ \mathrm{eV/kT}} \tag{A7}$$

[78] For the oxygen fugacity $f_{\mathrm{O_2}}$, the widely used formulation of *Myers and Eugster* [1983] for a quartz-fayalite-magnetite (QFM) buffer was used:

$$\mathrm{f_{O_2}} = 10^{-2.44419/\mathrm{T}+13.296} \tag{A8}$$

A2. Electrical Conductivity in the Presence of Water According to *Karato* [1990]

[79] *Karato* [1990] proposed that in the presence of aqueous fluids, dissolved hydrogen causes a significant reduction in the electrical resistivity of olivine, caused by charge transport through protons and/or enhanced diffusion of Mg^{2+} and Fe^{2+} ions in the presence of hydrogen. In this case, the conductivity can be described by a Nernst-Einstein relationship:

$$\sigma = \frac{cDq^2}{kT} \tag{A9}$$

where c is the hydrogen concentration, D is the hydrogen diffusivity, q is the hydrogen charge, k is the Boltzmann constant, and T is the temperature.

[80] Following the approach of *Lizarralde et al*. [1995], the effects of hydrogen diffusion on electrical resistivity can be determined using laboratory measurements of the diffusivity and solubility in olivine, as outlined below.

[81] The maximum hydrogen concentration can be estimated using laboratory measurements on hydrogen solubility $[H^+]_{\mathrm{ppm\ Si}}$ in olivine for temperatures of 1100°C and 1300°C and pressures (P) up to 12 GPa [*Bai and Kohlstedt*, 1992; *Kohlstedt et al*., 1996], which can be fit by a linear regression of $\log([H^+]_{\mathrm{ppm\ Si}})$ versus $\log(P)$ [*Lizarralde et al*., 1995]:

$$[H^+]_{\mathrm{ppm\ Si}} = 10^{-0.61\pm0.04}P^{1.19\pm0.01}\ (\mathrm{MPa}) \tag{A10}$$

[82] Laboratory measurements of hydrogen diffusivity D in olivine at temperatures (T) between 800°C and 1100°C and a pressure of 0.30 GPa indicate an anisotropic behavior, with the diffusivity along the three crystallographic axes being described by an Arrhenius relationship [*Mackwell and Kohlstedt*, 1990]:

$$D_a = (6\pm3)10^{-5}e^{-\frac{130\pm30}{RT}} \tag{A11}$$

$$D_b = (5\pm4)10^{-6}e^{-\frac{130\pm30}{RT}} \tag{A12}$$

$$D_c \approx 0.01D_a \tag{A13}$$

[83] Based on these laboratory measurements, the electrical conductivity for each of the three crystallographic directions can be calculated for varying temperatures and pressures. For comparison with the electrical resistivity models, it is necessary to calculate the isotropic average of the electrical conductivity. Several spatial averaging methods have been suggested to calculate this (see *Shankland and Duba* [1990] for a comparison), and in our analysis we use the effective medium theory by *Landauer* [1952]:

$$\sigma_{EM} = \frac{1}{4}\Bigg((3f_1-1)\sigma_1 + (3f_2-1)\sigma_2) + \left(((3f_1-1)\sigma_1 + (3f_2-1)\sigma_2)^2 + 8\sigma_1\sigma_2\right)^{\frac{1}{2}}\Bigg) \tag{A14}$$

with $f_1 = f_2 = 0.5$. σ_1 and σ_2 are set to be the serial and parallel averages σ_s and σ_p, respectively, which can be calculated as

$$\sigma_s^{-1} = \frac{1}{3}\left(\sigma_a^{-1} + \sigma_b^{-1} + \sigma_c^{-1}\right) \tag{A15}$$

$$\sigma_p = \frac{1}{3}(\sigma_a + \sigma_b + \sigma_c) \tag{A16}$$

where σ_a, σ_b, and σ_c correspond to the conductivities along the three crystallographic axes.

A3. Electrical Conductivity in the Presence of Water [*Wang et al*., 2006]

[84] *Wang et al*. [2006] investigated the Nernst-Einstein relationship (A9) through laboratory measurements on San Carlos olivine, which revealed a strong dependence of conductivity on water content but only a modest dependence on temperature. Based on their measurements, they found that the electrical conductivity for wet olivine was given by

$$\sigma_H = AC_w^r e^{-\frac{H^*}{RT}} \tag{A17}$$

where C_w is the water content (in weight percent), A and r are constants, H^* is the activation enthalpy, and T is temperature. For wet olivine, the constants were found to be $A = 10^{(3.0\pm0.4)}\frac{S}{m}$ and $r = 0.62\pm0.15$; the activation enthalpy was found to be $H^* = 87\pm5\frac{kJ}{mol}$. At low temperatures, the observed conductivities are significantly higher than the ones calculated by *Karato* [1990]. In addition, the obtained activation enthalpy is smaller than the one for diffusion of hydrogen, leading *Wang et al*. [2006] to the conclusion that other conductivity mechanisms than the ones proposed by *Karato* [1990] are required.

A4. Electrical Conductivity in the Presence of Water [*Yoshino et al.*, 2009]

[85] More recent laboratory studies by *Yoshino et al.* [2009] investigated the electrical conductivity of hydrous iron-bearing olivine in terms of three conductivity mechanisms (i.e., ionic, hopping (small polaron), and proton conduction). Based on their results, the electrical resistivity of hydrous olivine can be expressed as the sum of the Arrhenian formulas describing each of the three conductivity mechanisms:

$$\sigma = \sigma_{0i}\exp\left(-\frac{H_i}{kT}\right) + \sigma_{0h}\exp\left(-\frac{H_h}{kT}\right) + \sigma_{0p}C_w\exp\left(-\frac{H^0 - \alpha C_w^{1/3}}{kT}\right) \tag{A18}$$

where σ_{0i}, σ_{0h}, and σ_{0p} are the preexponential factors for the three conductivity mechanisms, H_i and H_h are the activation enthalpies for ionic and hopping conduction, respectively, H^0 is the activation enthalpy for proton conduction at very low water contents, C_w is the water content (in weight percent), α is a geometrical factor, k is the Boltzmann constant, and T is the temperature. For San Carlos olivine, the preexponential factors were found to be $\sigma_{0i} = 10^{(4.73\pm0.53)}\frac{S}{m}$, $\sigma_{0h} = 10^{(2.98\pm0.85)}\frac{S}{m}$, and $\sigma_{0p} = 10^{(1.90\pm0.44)}\frac{S}{m}$; the activation enthalpies were found to be $H_i = 2.31 \pm 0.07eV$, $H_h = 1.71 \pm 0.04eV$, and $H^0 = 0.92 \pm 0.04eV$; the geometrical factor was found to be $\alpha = 0.16 \pm 0.02$. The laboratory studies by *Yoshino et al.* [2009] reported significantly lower electrical conductivities than *Wang et al.* [2006]. *Yoshino et al.* [2009] attributed the difference to the higher temperatures used by *Wang et al.* [2006], which caused dehydration of the olivine sample. As a result, their higher electrical conductivities might be partly due to an interstitial fluid rather than purely due to hydrous olivine.

Appendix B: A Modification of Archie's Law for Two Conducting Phases

[86] Several mixing models have been proposed to calculate the electrical conductivity of a multiphase system. One commonly used model to explain the electrical conductivity in the presence of a fluid phase is Archie's law. However, Archie's Law assumes that the electrical conductivity of the fluid phase is several orders of magnitude higher than the electrical conductivity of the solid rock matrix, such that the rock matrix does not contribute. While this is true for crustal rocks, this assumption is no longer valid at mantle depths due to the relatively low resistivity of the predominant mantle mineral olivine.

[87] *Glover et al.* [2000] presented a modification of Archie's law to account for two conducting phases. For two phases with conductivities σ_1 and σ_2 and volume fractions $1-\chi_2$ and χ_2, the effective electrical conductivity σ_{eff} is given by

$$\sigma_{\text{eff}} = \sigma_1(1-\chi_2)^{\frac{\log\left(1-\chi_2^m\right)}{\log(1-\chi_2)}} + \sigma_2\chi_2^m \tag{B1}$$

where m is the cementation factor of the second phase, associated with its connectivity. Large exponents ($m > 2$) correspond to a low electrical connectivity, while small exponents ($m < 2$) are indicative of a high electrical connectivity. The cementation factor p for the first phase is dependent on the cementation factor m and therefore does not appear explicitly in the equation above.

Appendix C: Reduced Mantle Solidus in the Presence of Water

[88] The effect of water on the mantle solidus can be determined using cryoscopic calculations [*Hirschmann et al.*, 2009]. In a first step, it is necessary to determine the solidus temperature T of a dry peridotite mantle as a function of pressure P. Based on laboratory measurements, it can be parameterized as [*Hirschmann*, 2000; *Hirschmann et al.*, 2009]

$$T(^\circ\text{C}) = -5.104P^2 + 132.899P + 1120.661 \text{ for } P < 10 \text{ GPa} \tag{C1}$$

$$T(^\circ\text{C}) = -1.092(P-10)^2 + 32.39(P-10) + 1935 \text{ for } 10 \text{ GPa} < P < 23.5 \text{ GPa} \tag{C2}$$

$$T(^\circ\text{C}) = 26.53(P-23.5) + 2175 \text{ for } P > 23.5 \text{ GPa} \tag{C3}$$

[89] For temperatures greater than the solidus, the peridotite undergoes partial melting. If any water is present during this process, it will redistribute between the solid phase and the melt phase. This partition is described by the melt partition coefficient $D_H^{perid/liq}$

$$D_H^{perid/liq} = X_{ol}D_H^{ol/liq} + X_{opx}D_H^{opx/liq} + X_{cpx}D_H^{cpx/liq} + X_{gt}D_H^{gt/liq} + X_{spn}D_H^{spn/liq} \tag{C4}$$

and depends on the modal proportion X_i and the melt partition coefficient $D_H^{i/liq}$ of each of the mantle minerals olivine (ol), orthopyroxene (opx), clinopyroxine (cpx), garnet (gt), and spinel (spn).

[90] Melting can either occur through batch melting or fractional melting. For batch melting, the melt phase stays in contact with the residual rock crystal. Therefore, the overall bulk composition of the system remains the same. In contrast, for fractional melting, the melt phase is removed from the system due to density differences, leading to a continuously changing bulk composition.

[91] For the following calculations, batch melting is assumed, in which case the concentration of the water in the melt phase $C_{\text{H}_2\text{O}}^{\text{melt}}$ is given by

$$C_{\text{H}_2\text{O}}^{\text{melt}} = \frac{C_{\text{H}_2\text{O}}^0}{D_H^{perid/liq}(1-F)+F} \tag{C5}$$

where $C_{\text{H}_2\text{O}}^0$ is the bulk water concentration and F is the degree of melting. The concentration of the water in the residual rock crystal $C_{\text{H}_2\text{O}}^{\text{perid}}$ is given by

$$C_{\text{H}_2\text{O}}^{\text{perid}} = \frac{C_{\text{H}_2\text{O}}^0 D_H^{perid/liq}}{D_H^{perid/liq} + F\left(1 - D_H^{perid/liq}\right)} \tag{C6}$$

[92] *Aubaud et al.* [2004] have used a cryoscopic approach (i.e., determination of the freezing or melting point) based on empirical and thermodynamic calculations to estimate the effect of water on the solidus temperature. The reduced solidus temperature T for a given amount of

water, which is assumed to be completely dissociated to hydroxyl $X_{OH^-}^{melt}$, compared to the dry case T_{perid}^{fusion} is given by

$$T = \frac{T_{perid}^{fusion}}{\left(1 - \frac{R}{\Delta \hat{S}_{perid}^{fusion}} \ln\left(1 - X_{OH^-}^{melt}\right)\right)} \quad \text{(C7)}$$

where $\Delta \hat{S}_{perid}^{fusion}$ is the molar entropy of fusion. The molar entropy of fusion can be related to the entropy of fusion per unit mass $\Delta S_{perid}^{fusion}$ through

$$\Delta \hat{S}_{perid}^{fusion} = M \Delta S_{perid}^{fusion} \quad \text{(C8)}$$

where M is the number of grams in one mole of silicate.

[93] Of particular importance in the above calculations is the conversion from the amount of water as mass fraction (i.e., in weight percent) to hydroxyl mole fraction. As water partitions into the melt phase, part of the total amount of dissolved water H_2O_t reacts with oxygen atoms in the melt to form OH groups, leading to an equilibrium [*Zhang*, 2008]:

$$H_2O\ (melt) + O(melt) \leftrightarrow 2OH(melt) \quad \text{(C9)}$$

[94] In terms of mole fractions, this reaction can be written as

$$[H_2O_t] = [H_2O_m] + \frac{1}{2}[OH] \quad \text{(C10)}$$

[95] If we assume that all the water in the melt phase dissociates to OH, its mole fraction is related to the total amount of dissolved water through

$$[OH] = 2\,[H_2O_t] \quad \text{(C11)}$$

[96] There are three possible definitions on how the mole fraction of the total amount of dissolved water can be calculated, based on whether the oxygen is treated as one, two/three, or eight units [*Zhang*, 2008]:

[97] 1. For a single oxygen basis, the mole fraction of the total amount of water is given as

$$[H_2O_t] = \frac{\frac{C}{18.015}}{\frac{C}{18.015} + \frac{(1-C)}{W}} \quad \text{(C12)}$$

where C is the mass fraction of the total amount of water and W is the mass of the dry rock per mole of oxygen.

[98] 2. An alternative is to treat each oxide (e.g., SiO_2, Al_2O_3) as one unit. In this case the mole fraction of the total amount of water is given by

$$[H_2O_t] = \frac{\frac{C}{18.015}}{\sum \frac{C_i}{W_i}} \quad \text{(C13)}$$

where C_i and W_i are the mass fraction and molar mass of each oxide component, respectively.

[99] 3. In the eight oxygen basis, an eight oxygen molecule like $NaAlSi_3O_8$ is considered and treated as one unit. In this case the mole fraction of the total amount of water is given by

$$[H_2O_t] = \frac{\frac{C}{18.015}}{\frac{C}{18.015} + \frac{(1-C)}{W}} \quad \text{(C14)}$$

where W is the molar mass of the eight oxygen molecule (262.22 for $NaAlSi_3O_8$).

[100] **Acknowledgments.** This study was made possible by grants to Martyn Unsworth from the Natural Sciences and Engineering Research Council of Canada (NSERC), the Canada Foundation for Innovation (CFI), and the Alberta Ingenuity Fund (AIF). Ted Bertrand, Wolfgang Soyer, Volkan Tuncer, and Erşan Türkoğlu are thanked for their assistance with fieldwork. Technical support by Barry Narod is acknowledged. We thank members of the Lithoprobe project for permission to use their data. Gary Egbert is thanked for the use of his time series processing software and Randy Mackie for the use of his inversion algorithm. We thank Alan Jones and Gary McNeice for the use of the Strike program used for tensor decomposition. This paper benefited from reviews by the Associate Editor, Brad Hacker, and one anonymous reviewer.

References

Archie, G. E. (1942), The electrical resistivity log as an aid in determining some reservoir characteristics, *Trans. Am. Inst. Min. Metall. Pet. Eng.*, *146*, 54–62.

Aubaud, C., E. H. Hauri, and M. M. Hirschmann (2004), Hydrogen partition coefficients between nominally anhydrous minerals and basaltic melts, *Geophys. Res. Lett.*, *31*, L20611, doi:10.1029/2004GL021341.

Bai, Q., and D. L. Kohlstedt (1992), Substantial hydrogen solubility in olivine and implications for water storage in the mantle, *Nature*, *357*(6380), 672–674.

Bell, D. R., G. R. Rossman, J. Maldener, D. Endisch, and F. Rauch (2003), Hydroxide in olivine: A quantitative determination of the absolute amount and calibration of the IR spectrum, *J. Geophys. Res.*, *108*(B2), 2105, doi:10.1029/2001JB000679.

Black, P. R., and L. W. Braile (1982), Pn velocity and cooling of the continental lithosphere, *J. Geophys. Res.*, *87*(B13), 10,557–10,568.

Bostock, M. G., R. D. Hyndman, S. Rondenay, and S. M. Peacock (2002), An inverted continental Moho and serpentinization of the forearc mantle, *Nature*, *417*(6888), 536–8.

Bürgmann, R., and G. Dresen (2008), Rheology of the lower crust and upper mantle: Evidence from rock mechanics, geodesy, and field observations, *Annu. Rev. Earth Planet. Sci.*, *36*(1), 531–567.

Cammarano, F., S. Goes, P. Vacher, and D. Giardini (2003), Inferring upper-mantle temperatures from seismic velocities, *Phys. Earth Planet. In.*, *138*(3–4), 197–222.

Chapman, D. S. (1986), Thermal gradients in the continental crust, *Geol. Soc. London. Spec. Publ.*, *24*(1), 63–70.

Christensen, N. I., and W. D. Mooney (1995), Seismic velocity structure and composition of the continental crust: A global view, *J. Geophys. Res.*, *100*(B6), 9761.

Clowes, R. M., C. A. Zelt, J. R. Amor, and R. M. Ellis (1995), Lithospheric structure in the southern Canadian Cordillera from a network of seismic refraction lines, *Can. J. Earth Sci.*, *32*(10), 1485–1513.

Constable, S. (2006), SEO3: A new model of olivine electrical conductivity, *Geophys. J. Int.*, *166*(1), 435–437.

Cook, F. A., R. M. Clowes, D. B. Snyder, A. J. van der Velden, K. W. Hall, P. Erdmer, and C. A. Evenchick (2004), Precambrian crust beneath the Mesozoic northern Canadian Cordillera discovered by Lithoprobe seismic reflection profiling, *Tectonics*, *23*, TC2010, doi:10.1029/2002TC001412.

Cook, F. A., D. J. White, A. G. Jones, D. W. S. Eaton, J. Hall, and R. M. Clowes (2010), How the crust meets the mantle: Lithoprobe perspectives on the Mohorovičić discontinuity and crust–mantle transition, *Can. J. Earth Sci.*, *47*(4), 315–351.

Currie, C. A., and R. D. Hyndman (2006), The thermal structure of subduction zone back arcs, *J. Geophys. Res.*, *111*, B08404, doi:10.1029/2005JB004024.

Currie, C., K. Wang, R. D. Hyndman, and J. He (2004), The thermal effects of steady-state slab-driven mantle flow above a subducting plate: The Cascadia subduction zone and backarc, *Earth Planet. Sci. Lett.*, *223*(1–2), 35–48.

Dixon, J. E., T. H. Dixon, D. R. Bell, and R. Malservisi (2004), Lateral variation in upper mantle viscosity: Role of water, *Earth Planet. Sci. Lett.*, *222*(2), 451–467.

Egbert, G. D. (1997), Robust multiple-station magnetotelluric data processing, *Geophys. J. Int.*, *130*(2), 475–496.

Frederiksen, A. W., M. G. Bostock, and J. F. Cassidy (2001), S-wave velocity structure of the Canadian upper mantle, *Phys. Earth Planet. In.*, *124*(3–4), 175–191.

Gamble, T. D., W. M. Goubau, and J. Clarke (1979), Magnetotellurics with a remote magnetic reference, *Geophysics*, *44*(1), 53.

Glover, P. W. J., M. J. Hole, and J. Pous (2000), A modified Archie's law for two conducting phases, *Earth Planet. Sci. Lett.*, *180*(3–4), 369–383.

Gough, D. I. (1986), Mantle upflow tectonics in the Canadian Cordillera, *J. Geophys. Res.*, *91*(B2), 1909–1919.

Green, A. G., R. M. Clowes, C. J. Yorath, C. Spencer, E. R. Kanasewich, M. T. Brandon, and A. Sutherland Brown (1986), Seismic reflection imaging of the subducting Juan de Fuca plate, *Nature*, *319*(6050), 210–213.

Griffin, W., S. Y. O'Reilly, N. Abe, S. Aulbach, R. M. Davies, N. J. Pearson, B. J. Doyle, and K. Kivi (2003), The origin and evolution of Archean lithospheric mantle, *Precambrian Res.*, *127*(1–3), 19–41.

Groom, R. W., and R. C. Bailey (1989), Decomposition of magnetotelluric impedance tensors in the presence of local three-dimensional galvanic distortion, *J. Geophys. Res.*, *94*(B2), 1913–1925.

Guo, X., T. Yoshino, and I. Katayama (2011), Electrical conductivity anisotropy of deformed talc rocks and serpentinites at 3GPa, *Phys. Earth Planet. In.*, *188*(1–2), 69–81.

Hacker, B. R. (2008), H_2O subduction beyond arcs, *Geochem. Geophys. Geosyst.*, *9*, Q03001, doi:10.1029/2007GC001707.

Hirschmann, M. M. (2000), Mantle solidus: Experimental constraints and the effects of peridotite composition, *Geochem. Geophys. Geosyst.*, *1*(10), doi:10.1029/2000GC000089.

Hirschmann, M. M., T. Tenner, C. Aubaud, and A. C. Withers (2009), Dehydration melting of nominally anhydrous mantle: The primacy of partitioning, *Phys. Earth Planet. In.*, *176*(1–2), 54–68.

Honda, S., M. Saito, and T. Nakakuki (2002), Possible existence of small-scale convection under the back arc, *Geophys. Res. Lett.*, *29*(21), 2043, doi:10.1029/2002GL015853.

Hyndman, R. D. (1988), Dipping seismic reflectors, electrically conductive zones, and trapped water in the crust over a subducting plate, *J. Geophys. Res.*, *93*(B11), 13,391–13,405.

Hyndman, R. D., and C. A. Currie (2011), Why is the North America Cordillera high? Hot backarcs, thermal isostasy, and mountain belts, *Geology*, *39*(8), 783–786.

Hyndman, R. D., and T. J. Lewis (1999), Geophysical consequences of the Cordillera–Craton thermal transition in southwestern Canada, *Tectonophysics*, *306*(3–4), 397–422.

Hyndman, R. D., and S. M. Peacock (2003), Serpentinization of the forearc mantle, *Earth Planet. Sci. Lett.*, *212*(3–4), 417–432.

Hyndman, R. D., C. A. Currie, S. Mazzotti, and A. Frederiksen (2009), Temperature control of continental lithosphere elastic thickness, Te vs Vs, *Earth Planet. Sci. Lett.*, *277*(3–4), 539–548.

Jones, A. G. (1983), The problem of current channelling: A critical review, *Geophys. Surv.*, *6*(1–2), 79–122.

Jones, A. G., and D. I. Gough (1995), Electromagnetic images of crustal structures in southern and central Canadian Cordillera, *Can. J. Earth Sci.*, *32*(10), 1541–1563.

Karato, S. (1990), The role of hydrogen in the electrical conductivity of the upper mantle, *Nature*, *347*(6290), 272–273.

Karato, S.-I. (2006), Remote sensing of hydrogen in Earth's mantle, *Rev. Mineral. Geochem.*, *62*(1), 343–375.

Karato, S.-I., M. S. Paterson, and J. D. Fitzgerald (1986), Rheology of synthetic olivine aggregates: Influence of grain size and water, *J. Geophys. Res.*, *91*(B8), 8151–8176.

Kohlstedt, D. L., and M. E. Zimmerman (1996), Rheology of partially molten mantle rocks, *Annu. Rev. Earth Planet. Sci.*, *24*(1), 41–62.

Kohlstedt, D. L., H. Keppler, and D. C. Rubie (1996), Solubility of water in the α, β and γ phases of (Mg,Fe) 2 SiO 4, *Contrib. Mineral. Petrol.*, *123*(4), 345–357.

Kurtz, R. D., J. M. DeLaurier, and J. C. Gupta (1986), A magnetotelluric sounding across Vancouver Island detects the subducting Juan de Fuca plate, *Nature*, *321*(6070), 596–599.

Kurtz, R. D., J. M. DeLaurier, and J. C. Gupta (1990), The electrical conductivity distribution beneath Vancouver Island: A region of active plate subduction, *J. Geophys. Res.*, *95*(B7), 10,929–10,946.

Landauer, R. (1952), The electrical resistance of binary metallic mixtures, *J. Appl. Phys.*, *23*(7), 779.

Ledo, J., and A. G. Jones (2001), Regional electrical resistivity structure of the southern Canadian Cordillera and its physical interpretation, *J. Geophys. Res.*, *106*(B12), 30,755–30,769.

Lewis, T. J., W. H. Bentkowski, E. E. Davis, R. D. Hyndman, J. G. Souther, and J. A. Wright (1988), Subduction of the Juan de Fuca plate: Thermal consequences, *J. Geophys. Res.*, *93*(B12), 15,207–15,225.

Lewis, T. J., W. H. Bentkowski, and R. D. Hyndman (1992), Crustal temperatures near the Lithoprobe Southern Canadian Cordillera Transect, *Can. J. Earth Sci.*, *29*(6), 1197–1214.

Lizarralde, D., A. Chave, G. Hirth, and A. Schultz (1995), Northeastern Pacific mantle conductivity profile from long-period magnetotelluric sounding using Hawaii-to-California submarine cable data, *J. Geophys. Res.*, *100*(B9), 17,837–17,854.

Mackwell, S. J., and D. L. Kohlstedt (1990), Diffusion of hydrogen in olivine: Implications for water in the mantle, *J. Geophys. Res.*, *95*(B4), 5079–5088.

Marquis, G., and R. D. Hyndman (1992), Geophysical support for aqueous fluids in the deep crust: seismic and electrical relationships, *Geophys. J. Int.*, *110*(1), 91–105.

McNeice, G. W., and A. G. Jones (2001), Multisite, multifrequency tensor decomposition of magnetotelluric data, *Geophysics*, *66*(1), 158.

Mercier, J., M. G. Bostock, J. F. Cassidy, K. Dueker, J. B. Gaherty, E. J. Garnero, J. Revenaugh, and G. Zandt (2009), Body-wave tomography of western Canada, *Tectonophysics*, *475*(3–4), 480–492.

Monger, J., and R. Price (2002), The Canadian Cordillera: Geology and tectonic evolution, *CSEG Recorder*, 17–36.

Myers, J., and H. P. Eugster (1983), The system Fe-Si-O: Oxygen buffer calibrations to 1,500 K, *Contrib. Mineral. Petrol.*, *82*(1), 75–90.

Ni, H., H. Keppler, and H. Behrens (2011), Electrical conductivity of hydrous basaltic melts: implications for partial melting in the upper mantle, *Contrib. Mineral. Petrol.*, 162(3), 637–650.

Nicholson, T., M. Bostock, and J. F. Cassidy (2005), New constraints on subduction zone structure in northern Cascadia, *Geophys. J. Int.*, *161*(3), 849–859.

Parkinson, W. D. (1962), The influence of continents and oceans on geomagnetic variations, *Geophys. J. Int.*, *6*(4), 441–449.

Parkinson, W. D., and F. W. Jones (1979), The geomagnetic coast effect, *Rev. Geophys.*, *17*(8), 1999.

Paterson, M. S. (1982), The determination of hydroxyl by infrared absorption in quartz, silicate glasses and similar materials, *Bull. Minéral.*, *105*, 20–29.

Reynard, B., K. Mibe, and B. V. de Moortèle (2011), Electrical conductivity of the serpentinised mantle and fluid flow in subduction zones, *Earth Planet. Sci. Lett.*, *307*(3–4), 387–394.

Riddihough, R. P. (1979), Gravity and structure of an active margin—British Columbia and Washington, *Can. J. Earth Sci.*, *16*(2), 350–363.

Rodi, W., and R. L. Mackie (2001), Nonlinear conjugate gradients algorithm for 2-D magnetotelluric inversion, *Geophysics*, *66*(1), 174.

Ross, J. (1983), The nature and rheology of the cordilleran upper mantle of british columbia: Inferences from peridotite xenoliths, *Tectonophysics*, *100*(1–3), 321–357.

Rudnick, R. L., W. F. McDonough, and R. J. O'Connell (1998), Thermal structure, thickness and composition of continental lithosphere, *Chem. Geol.*, *145*(3–4), 395–411.

Rüpke, L. H., J. P. Morgan, M. Hort, and J. A. D. Connolly (2004), Serpentine and the subduction zone water cycle, *Earth Planet. Sci. Lett.*, *223*(1–2), 17–34.

Saruwatari, K., S. Ji, L. Changxing, and M. H. Salisbury (2001), Seismic anisotropy of mantle xenoliths and constraints on upper mantle structure beneath the southern Canadian Cordillera, *Tectonophysics*, *339*(3–4), 403–426.

Shankland, T. J., and A. G. Duba (1990), Standard electrical conductivity of isotropic, homogeneous olivine in the temperature range 1200°–1500°C, *Geophys. J. Int.*, *103*(1), 25–31.

Simpson, F., and K. Bahr (2005), *Practical Magnetotellurics*, 272 pp., Cambridge University Press, Cambridge, U.K.

Soyer, W., and M. Unsworth (2006), Deep electrical structure of the northern Cascadia (British Columbia, Canada) subduction zone: Implications for the distribution of fluids, *Geology*, *34*(1), 53–56.

Spence, G. D., R. M. Clowes, and R. M. Ellis (1985), Seismic structure across the active subduction zone of western Canada, *J. Geophys. Res.*, *90*(B8), 6754.

ten Grotenhuis, S. M., M. R. Drury, C. J. Spiers, and C. J. Peach (2005), Melt distribution in olivine rocks based on electrical conductivity measurements, *J. Geophys. Res.*, *110*(B12), B12201, doi:10.1029/2004JB003462.

Türkoğlu, E., M. Unsworth, and D. Pana (2009), Deep electrical structure of northern Alberta (Canada): Implications for diamond exploration, *Can. J. Earth Sci.*, *46*(2), 139–154.

Tyburczy, J. A., and H. S. Waff (1983), Electrical conductivity of molten basalt and andesite to 25 kilobars pressure: Geophysical significance and implications for charge transport and melt structure, *J. Geophys. Res.*, *88*(B3), 2413–2430.

Unsworth, M., and S. Rondenay (2013), Mapping the distribution of fluids in the crust and lithospheric mantle utilizing geophysical methods, in *Metasomatism and the Chemical Transformation of Rock*, edited bySpinger, Berlin Heidelberg, pp. 535–598.

van der Lee, S., and A. Frederiksen (2005), Surface wave tomography applied to the North American upper mantle, *Geophys. Monogr. Ser.*, *157*, 67–80.

Wada, I., K. Wang, J. He, and R. D. Hyndman (2008), Weakening of the subduction interface and its effects on surface heat flow, slab dehydration, and mantle wedge serpentinization, *J. Geophys. Res.*, *113*, B04402, doi:10.1029/2007JB005190.

Wang, D., M. Mookherjee, X. S. Xu, and S. Karato (2006), The effect of water on the electrical conductivity of olivine, *Nature*, *443*(7114), 977–80.

Watanabe, T., M. G. Langseth, and R. N. Anderson (1977), Heat flow in back-arc basins of the Western Pacific, in *Island Arcs, Deep Sea Trenches and Back-Arc Basins, Maurice Ewing Series*, edited by M. Talwani, and W. C. Pitman, pp. 137–161, American Geophysical Union, Washington, D.C.

Xu, Y., T. Shankland, and A. Duba (2000), Pressure effect on electrical conductivity of mantle olivine, *Phys. Earth Planet. In.*, *118*(1–2), 149–161.

Yoshino, T., T. Matsuzaki, A. Shatskiy, and T. Katsura (2009), The effect of water on the electrical conductivity of olivine aggregates and its implications for the electrical structure of the upper mantle, *Earth Planet. Sci. Lett.*, *288*(1–2), 291–300.

Zhang, Y. (2008), *Geochemical Kinetics*, 656 pp., Princeton University Press, Princeton, N.J.